

# Deep reinforcement learning-based active flow control of an elliptical cylinder: transitioning from an elliptical cylinder to a circular cylinder and a flat plate

Wang Jia (贾旺)<sup>1</sup> and Hang Xu (徐航)<sup>1</sup>

*State Key Lab of Ocean Engineering, School of Naval Architecture, Ocean and Civil Engineering, Shanghai Jiao Tong University, Shanghai, 200240, China*

(\*Electronic mail: hangxu@sjtu.edu.cn)

(Dated: 30 April 2024)

This study investigates the effectiveness of active flow control (AFC) technology supported by deep reinforcement learning (DRL) applied to flows around elliptical cylinders at  $Re = 100$ . We vary the aspect ratio ( $Ar$ ) of the elliptical cylinder from an ellipsoid ( $Ar = 2.0$ ) to a circular shape ( $Ar = 1.0$ ), and ultimately to a flat plate ( $Ar = 0$ ). We utilize the proximal policy optimization (PPO) algorithm to precisely control the mass flow rates of synthetic jets located on both the upper and lower surfaces of the cylinder. The control objective focuses on reducing drag, minimizing lift and suppressing vortex shedding. We examine the robustness and adaptability of DRL-based control techniques across different geometric configurations. Our research findings indicate that, for elliptical cylinders with  $Ar$  between 1.75 and 0.75, the reduction in drag coefficient ranges from 0.9% to 15.7%, and the reduction in lift coefficient ranges from 95.2% to 99.7%. Notably, the DRL-based control strategy not only significantly reduces lift and drag, but also completely suppresses vortex shedding while using less than 1% of external excitation energy, demonstrating its efficiency and energy-saving capabilities. Additionally, for  $Ar$  from 0.5 to 0, the reduction in drag coefficient ranges from 26.9% to 43.6%, and the reduction in lift coefficient from 50.2% to 68.0%. This reflects the control strategy's significant reduction in both drag and lift coefficients, while also alleviating vortex shedding. Overall, our findings underscore the adaptability and potential of DRL-based AFC in controlling complex fluid dynamics across diverse geometric configurations.

## I. INTRODUCTION

The development of active flow control (AFC) technology has progressed from theoretical exploration to practical application, gradually becoming an important branch within the domains of fluid mechanics and engineering.<sup>1-3</sup> This technology actively intervenes the flow field to improve flow characteristics, such as reducing drag, controlling vortex shedding, enhancing mixing efficiency, or preventing flow separation, thereby enhancing system performance and efficiency.<sup>1,4</sup> In its early stages, AFC research primarily focused on theoretical analysis and simple experiments to explore the influence of external inputs, such as jets, vibrations, or magnetic fields, on fluid flow dynamics.<sup>2-4</sup> With the advancement of computational fluid dynamics (CFD) and increased computational power, researchers have been able to delve deeper into complex flow responses through numerical simulations and develop more effective control strategies.<sup>5-7</sup> However, as fluid problems are typically characterized by a high degree of nonlinearity and multiscale nature, involving high-dimensional state spaces and complex system dynamics<sup>8,9</sup>, many engineering problems are often intractable using existing models. Sophisticated control strategies that require consideration of a wide range of spatiotemporal scales are indispensable when addressing phenomena such as unstable flows, turbulence, and multiphase flows.<sup>10</sup>

Recently, the field of AFC has witnessed revolutionary progress, thanks to breakthroughs in machine learning and deep learning technologies.<sup>11-13</sup> Deep reinforcement learning (DRL) is an avant-garde technique that combines the principles of deep learning with reinforcement learning to optimize decision-making through interactions with an environment.<sup>14-16</sup> Deep learning excels at autonomously extracting intricate features from voluminous datasets, while reinforcement learning concentrates on how to make optimal decisions based on these features by guiding the learning process through rewards.<sup>17,18</sup> By utilizing deep neural networks to represent policies or value functions within reinforcement learning, DRL enables machines to tackle complex decision-making challenges and high-dimensional state spaces that were previously considered intractable.<sup>14-16</sup> Renowned for its robust non-linear modeling capabilities and adaptive learning mechanisms, DRL has the capability to directly learn complex strategies from raw sensory data without relying on manually engineered features.<sup>19</sup> Furthermore, DRL is inherently self-improving, continuously refining its strategies through ongoing interactions with the environment.<sup>16</sup> The self-learning and adaptive nature of DRL grants a significant advantage, particularly in resolving decision-making problems in dynamic settings.<sup>15,16</sup> The applications of DRL are vast and encompass various domains, including gaming, autonomous vehicles, robotic control, natural language processing, and computer vision. In the gaming industry, distinguished achievements like AlphaGo's victory over world champions highlight the potential of DRL.<sup>20</sup> In the realm of autonomous driving, DRL is employed to optimize route planning and decision-making.<sup>21</sup> In the field of robotics, it enables robots to learn complex physical tasks.<sup>22</sup> Overall, DRL offers the potential to develop adaptive and intelligent control strategies that can adapt to changing environments and optimize performance in a wide range of applications.

With progressive advancement in the DRL technology, there has been a significant increase in the application of DRL in the field of fluid dynamics as well.<sup>11,12,23,24</sup> DRL methods are highly suited to handle the high-dimensional and complex state spaces intrinsic to fluid dynamics.<sup>25</sup> Through the function approximation capabilities of deep neural networks, DRL is adept at processing fluid systems and discerning flow patterns and structures.<sup>26</sup> DRL models, through their interaction with the environment and trial-and-error processes, can independently learn and refine strategies to meet diverse fluid conditions.<sup>1,2,27</sup> For instance, DRL has been applied to shape optimization of fluid systems and enabled automatic discovery and application of effective shape adjustments to achieve optimization goals by intelligently exploring the design space and learning optimal strategies.<sup>28</sup> Moreover, the long-term reward mechanism intrinsic to DRL allows for the consideration of future impacts when formulating strategies. This unique feature has allowed DRL to shine in many AFC problems where DRL's focus on long-term rewards enables control models to balance short-term gains with future outcomes, thereby better addressing control and optimization challenges within fluid mechanics.<sup>29-32</sup>

In the academic literature, flow control around blunt bodies using DRL has attracted considerable interest due to its pivotal role in reducing drag, a key aspect of fluid dynamics research. This pursuit carries several important implications, including enhanced energy efficiency, improved performance, noise and vibration reduction, and industrial process optimization. As flow around blunt body tends to involve strong non-linearities such as flow separation and recirculation, traditional control methods often struggle in achieving control objectives whereas DRL models have shown promising results. Pioneered by Rabault *et al.*<sup>33</sup>, various researchers such as Tang *et al.*<sup>34</sup>, Heess *et al.*<sup>35</sup>, Ren, Rabault, and Tang<sup>36</sup>, and Wang and Xu<sup>37</sup> applied the Proximal Policy Optimization (PPO) algorithm to AFC in the flow around a circular cylinder. Consistently, they achieved an approximate 8% reduction in drag in their validation experiments. Furthermore, Li and Zhang<sup>38</sup>, Wang *et al.*<sup>39</sup>, Jia and Xu<sup>40</sup>, and Wang *et al.*<sup>41</sup> respectively conducted flow control studies on confined circular cylinders and square cylinders using DRL. In addition, Fan *et al.*<sup>42</sup> initiated the application of DRL to AFC experiments, optimizing power efficiency by adjusting the rotational speed of auxiliary circular cylinders positioned behind another circular cylinder. Ren, Wang, and Tang<sup>43</sup> proposed an AFC strategy to conceal the hydrodynamic characteristics of circular cylinders, such as strong shear forces and periodic shedding vortices. Studies on flow around constrained circular cylinders under different blockage ratios have also received extensive attention in the field<sup>33,34,37-39</sup>. The existing studies have successfully demonstrated the effectiveness of using DRL for flow control, particularly in actively manipulating the flow around circular cylinders and square cylinders.

Although active flow control strategies for both circular and square cylinders are pivotal in various engineering applications for managing aerodynamic and hydrodynamic forces<sup>23,24,30,44</sup>, their extension to more intricate, non-ideal geometries poses significant challenges. The effectiveness of DRL strategies in such contexts remains largely unexplored, marked by uncertainties regarding their capacity to generate physically reasonable and adaptable control measures. Current literature indicates a distinct lack of comprehensive studies on the variability of DRL-based flow control strategies across different geometries, such as from streamlined bodies to various bluff bodies. This research proposes to bridge these gaps by focusing on the flow dynamics around parameterized ellipsoids, examining how variations in the aspect ratio influence flow fields and their corresponding DRL-driven control strategies. By extending the investigation from elongated ellipsoids to circular cylinders and subsequently normal flat plates, this study aims to develop a deeper understanding of the physical validity of DRL approaches and their adaptability across varying body geometries.

This work extends the studies conducted by Wang and Xu<sup>37,40</sup> by applying the DRL-based AFC approach to elliptical cylinders, which present more complex flow characteristics and additional control challenges. The objective is to develop effective control strategies to reduce drag, improve flow stability, and enhance overall performance. The structure of this paper is organized as follows: Sec. II introduces the problem description and provides a comprehensive overview of DRL and its framework for application in AFC. Sec. III presents the main results and analysis. Finally, Sec. IV concludes the paper by summarizing the key findings and discussing their implications.

## II. PROBLEM DESCRIPTION AND METHODOLOGY

### A. Numerical simulation

*a. Model configuration* We investigate the flow characteristics around a two-dimensional elliptical cylinder. As illustrated in Fig. 1(a), the flow is described using a coordinate system where the  $x$ -axis aligns with the flow direction, and the  $y$ -axis is the perpendicular direction. The origin of the coordinate system is set at the center of the elliptical cylinder, denoted as  $O$ . The computational domain extends from  $-2D$  ahead of the cylinder to  $20D$  behind it in the flow direction, where  $D$  represents a reference length. In the cross-flow direction, which is perpendicular to the flow, the domain spans from  $-2D$  to  $2.1D$ . The elliptical cylinder has one axis that remains fixed with a length of  $2a$  (equivalent to  $D$ ), while the other axis has a length of  $2b$ . The synthetic jets, symmetrically positioned at  $\theta_1 = 90^\circ$  and  $\theta_2 = 270^\circ$  on the elliptical cylinder, have a fixed jet opening width of  $\omega = 10^\circ$ , as depicted in Fig. 1(b). Let aspect ratio ( $Ar$ ) be the ratio of the semi-axis  $b$  to the semi-axis  $a$ . By adjusting its value, the elliptical cylinder can exhibit different shapes, as illustrated in Fig. 1(c). In particular,  $Ar = 0$  corresponds to a flat plate (thickness is  $0.05D$ ) perpendicular to the flow, while  $Ar = 1$  corresponds to a circular cylinder.

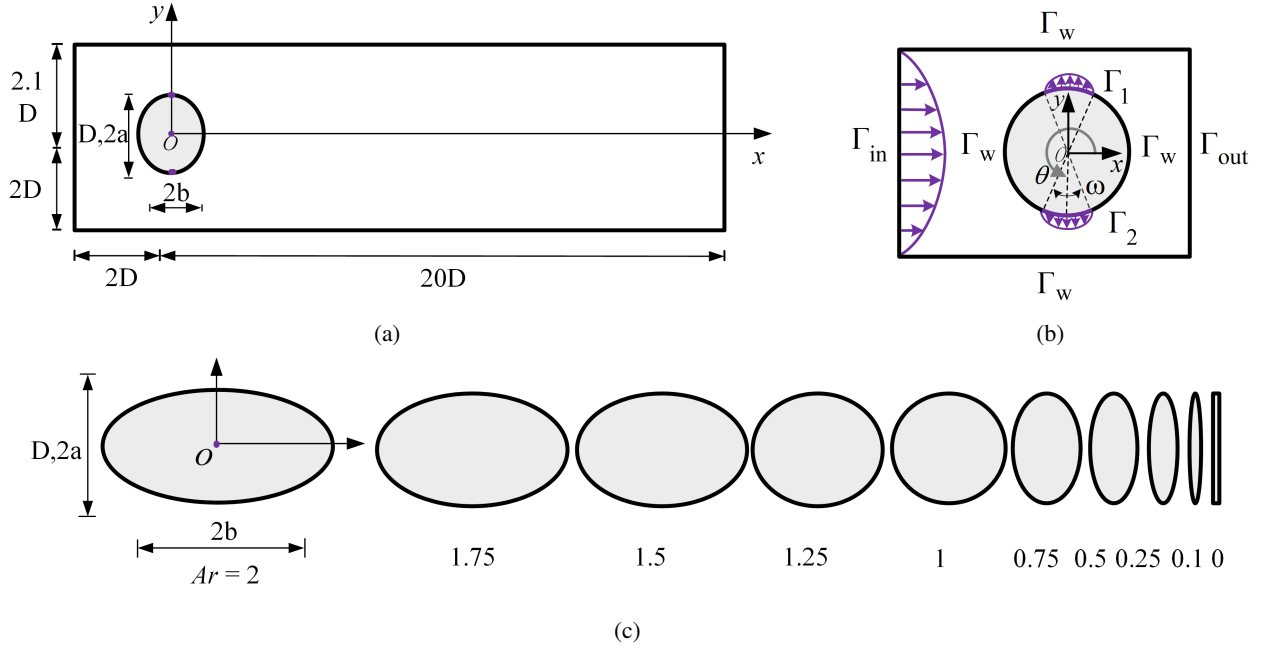


FIG. 1: (a) Definition of the problem, including the dimensions of the computational domain and the establishment of a Cartesian coordinate system. (b) Establishment of boundary conditions; note that the dimensions of the elliptical cylinder and the computational domain in the figure are not to scale, focusing solely on the delineation of boundary conditions. (c) This study investigates elliptical cylinders with different aspect ratio: a normal flat plate corresponding to  $Ar = 0$ , a circular cylinder with  $Ar = 1$ , and an elliptical cylinder with  $Ar = 2$ . The dimension  $2a$  is fixed as  $D$ , and the  $Ar$  is varied by changing the length of  $2b$ .

*b. Governing equations* Let  $\Omega \subset \mathbb{R}^{nd}$  and  $(0, T)$  be the spatial and temporal domains, respectively, where  $nd$  is the number of space dimensions, and let  $\Gamma$  denote the boundary of  $\Omega$ . The Navier-Stokes equations that describe the dynamics of this incompressible viscous fluid flow are given by:

$$\frac{\partial \mathbf{u}}{\partial t} + \mathbf{u} \cdot (\nabla \mathbf{u}) = -\nabla p + Re^{-1} \Delta \mathbf{u} \quad \text{on } \Omega \times (0, T), \quad (1a)$$

$$\nabla \cdot \mathbf{u} = 0 \quad \text{on } \Omega \times (0, T), \quad (1b)$$

where  $\mathbf{u}$ ,  $t$  and  $p$  are the velocity vector, time, and pressure, respectively. In this study, the  $Re$  is set to 100.

*c. Boundary conditions* The upstream boundary of the computational domain, designated as  $\Gamma_{in}$ , is characterized by a parabolic velocity profile oriented in the  $x$ -axis, where the boundary conditions are specified such that the transverse velocity component is set to zero, and the velocity along the stream direction shows a parabolic profile distribution. On the downstream boundary, denoted as  $\Gamma_{out}$ , a *Neumann-type* boundary condition is prescribed for the velocity field, ensuring that the stress vector is nullified. On the upper and lower boundaries  $\Gamma_w$ , a slip-wall boundary condition is employed, which stipulates that both the velocity component perpendicular to these boundaries and the tangential stress vector component along them are assigned a value of zero. The synthetic jets boundaries are denoted by  $\Gamma_i$  ( $i = 1, 2$ ). The velocity within the jets adheres to a parabolic distribution, with the sign of the jet velocity indicative of fluid suction or injection. The design of the synthetic jets ensures mass flow balance, as expressed by the condition  $V_{\Gamma_1} = -V_{\Gamma_2}$ , to maintain mass conservation in the system. Except for the synthetic jets, the non-slip solid wall boundary condition  $\Gamma_w$  is adopted for the rest of the cylinder.

In compliance with the above requirements, the system is considered with the following boundary conditions

$$\begin{aligned} -\rho \mathbf{n} \cdot \mathbf{p} + Re^{-1} (\mathbf{n} \cdot \nabla \mathbf{u}) &= 0 \quad \text{on } \Gamma_{out}, \\ \mathbf{u} &= 0 \quad \text{on } \Gamma_w, \\ \mathbf{u} &= U \quad \text{on } \Gamma_{in}, \\ \mathbf{u} &= f_{Q_i} \quad \text{on } \Gamma_i, \quad i = 1, 2. \end{aligned} \quad (2)$$

Here,  $U$  is the inflow velocity profile.  $f_{Q_i}$  represents the radial velocity profiles simulating the suction or injection of fluid by the jets. The specific formulas of  $U$  and  $f_{Q_i}$  will be given below.

At the inlet  $\Gamma_{in}$ , the inflow velocity  $U$  along the  $x$ -axis is prescribed by a parabolic velocity profile in the form,

$$U = U_m \frac{(H-2y)(H+2y)}{H^2}. \quad (3)$$

Here,  $U_m$  is the maximum velocity magnitude of the parabolic profile, and  $H = 4.1D$  represents the total height of the rectangular domain. The mean velocity magnitude is  $\bar{U} = 2U_m/3 = 1$  and is used to define the Reynolds number  $Re = \bar{U}D/\nu$ .

The functions  $f_{Q_i}$  represent radial velocity profiles that simulate the suction or injection mechanisms of the jets. These profiles are selected to ensure a smooth transition to the no-slip boundary conditions on the surfaces  $\Gamma_W$  of the cylinder. Specifically,  $f_{Q_i}$  is defined as  $A(\theta; Q_i)(x, y)$ , with the modulation relying on the angular coordinate  $\theta$  as illustrated in Fig. 2. For the jet characterized by a width of  $\omega$  and centered at  $\theta_0$ , which is positioned on the cylinder with radius  $R$ , the modulation is established as follows:

$$A(\theta; Q) = Q \frac{\pi}{2\omega R^2} \cos\left(\frac{\pi}{\omega}(\theta - \theta_0)\right). \quad (4)$$

*d. Solver details* In this study, the incompressible flow solver is based on the open-source CFD package OpenFOAM, as described by Jasak *et al.*<sup>45,46</sup> OpenFOAM is a widely used and validated CFD software package that provides robust numerical algorithms for solving the Navier-Stokes equations. The solver in OpenFOAM utilizes the finite volume method to discretize the computational domain into a mesh made up of control volumes. To ensure numerical stability, the time step is chosen as  $\Delta t = 0.0005$ .

*e. Grid system* Considering an elliptical cylinder computational domain with  $Ar = 1$ , the domain is discretized employing a hybrid meshing approach that integrates both structured (quadrilateral) and unstructured (triangular) meshes. As delineated in Fig. 2, the computational domain is divided into 18,484 mesh cells. Specifically, the area surrounding the elliptical cylinder is discretized using a multi-layer quadrilateral mesh, while the remaining regions are discretized with triangular meshes. Fig.2(a) displays the global discretization scheme for the computational domain, highlighting the comprehensive approach to mesh division. Fig.2(b) provides a detailed view of the mesh partitioning near the elliptical cylinder, where the multi-layered quadrilateral meshes surrounding the cylinder are notably finer compared to the triangular meshes. Fig.2(c) illustrates the division of multi-layered quadrilateral meshes around the elliptical cylinder, emphasizing the precision of discretization near the structure. Finally, fig.2(d) showcases the mesh division around the elliptical cylinder and the integration strategy between quadrilateral and triangular meshes. The method for mesh division for ellipses with  $Ar$  values other than 1 follows the same approach as that for  $Ar = 1$ , and is not separately demonstrated.

*f. Quantities of interest* The lift coefficient ( $C_L$ ) and drag coefficient ( $C_D$ ) are defined as

$$C_L = \frac{F_L}{0.5\rho\bar{U}^2D}, \quad C_D = \frac{F_D}{0.5\rho\bar{U}^2D}. \quad (5)$$

Here,  $F_L$  and  $F_D$  represent the lift and drag forces integrated on the surface of the elliptical cylinder, respectively, and  $\rho$  is the fluid density. The Strouhal number ( $St$ ) is used to describe the characteristic frequency of oscillatory flow phenomena and is defined as follows:

$$St = \frac{f_s \cdot D}{\bar{U}} \quad (6)$$

Where  $f_s$  is the shedding frequency calculated based on the periodic evolution of the  $C_L$ .  $D$  is the characteristic length of the elliptical cylinder, and  $\bar{U} = 1$ .

*g. Grid independence* Taking the case with an  $Ar$  of 1 as an example, this study explores mesh convergence and validates the numerical method utilized. Tab. I presents the simulation results using three meshes with differing resolutions, enabling a comparative analysis of the maximum drag coefficient  $C_{D,max}$ , the mean of the maximum drag coefficient  $C_{D,mean}$ , the maximum lift coefficient  $C_{L,max}$ , and the  $St$ . Furthermore, the results of the numerical simulations are compared with the findings of Rabault *et al.*<sup>33</sup> and Schäfer *et al.*<sup>47</sup> for validation. The simulations conducted using a coarse mesh revealed significant deviations in the drag and lift coefficients when compared to the results by Rabault *et al.*<sup>33</sup>, questioning the accuracy of such numerical simulations. On the other hand, the fine mesh, characterized by a high density of grid points, considerably slows down the training speed for reinforcement learning, presenting a challenge for efficient simulation execution. Our aim is to perform numerical simulations with the least number of mesh cells without compromising on computational accuracy. Consequently, the discretization strategy of the main mesh was adopted for subsequent numerical simulations and reinforcement learning training. This strategy not only satisfies the computational accuracy requirements but also keeps the mesh element count to a manageable level. Comparison of the computational results from the main mesh with those obtained by Rabault *et al.*<sup>33</sup> shows very little difference, indicating a high level of accuracy. Furthermore, the accuracy of the main mesh's results lies within the upper and lower bounds provided by standard benchmarks<sup>47</sup>, confirming that the computational precision of the main mesh is adequate for further training purposes. The above analysis ensures the best balance between numerical accuracy and computational efficiency. The methodology for examining mesh dependency for ellipses with  $Ar$  other than 1 is consistent with the procedure established for  $Ar = 1$ .

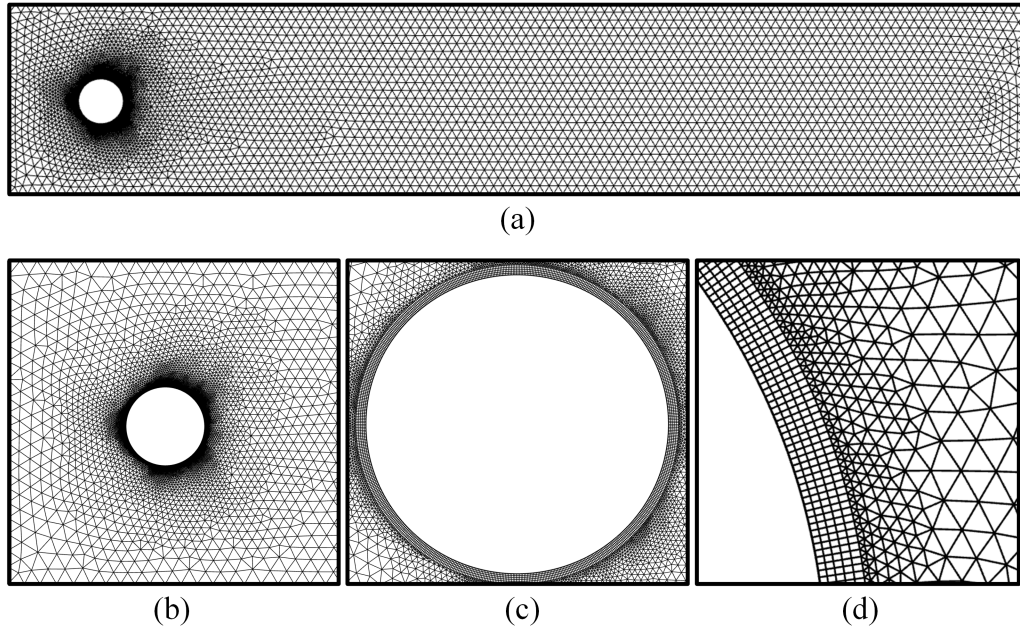


FIG. 2: For  $Ar = 1$ , the computational domain is discretized into 18,484 mesh cells, including both triangular and quadrilateral meshes. (a) Discretization of the computational domain is viewed from a global perspective. (b) A comprehensive display of the mesh around the elliptical cylinder. (c) Presentation of the multi-layered quadrilateral meshes surrounding the elliptical cylinder. (d) A magnified view of the quadrilateral meshes in the vicinity of the elliptical cylinder.

TABLE I: Grid independence test for an elliptical cylinder with  $Ar = 1$  at  $Re = 100$ .

Configuration	Mesh resolution	Mesh	$C_{D,max}$	$C_{D,mean}$	$C_{L,max}$	$St$
Schäfer <i>et al.</i> <sup>47</sup>	-	-	3.220–3.240	-	0.990–1.010	0.295–0.305
Rabault <i>et al.</i> <sup>33</sup>	-	9262		3.205	-	
$Ar = 1$	Coarse	10,540	3.242	3.224	1.052	0.304
	Medium	18,484	3.225	3.205	0.990	0.300
	Fine	25,624	3.228	3.207	0.992	0.301

## B. Deep Reinforcement learning

*a. Deep learning* Deep learning, a subset of machine learning, employs multi-layer artificial neural networks to model and learn intricate nonlinear relationships. Fig. 3 demonstrates how deep learning captures the representation of input data across multiple layers of a neural network, including the input layer, several hidden layers, and the output layer. Each layer is composed of numerous neural units, with information transmitted between nodes via connection weights. The fundamental concept behind deep learning is its ability to autonomously learn data representations through successive layers. Utilizing the backpropagation algorithm, the network autonomously discerns the transformation process from raw data to sophisticated, high-level abstract features, eliminating the need for manual feature extraction.

*b. Reinforcement learning* In the domain of Reinforcement Learning, the interaction between an agent and its environment is the core mechanism by which learning is facilitated. As illustrated in Figure 3, this interaction proceeds in a cyclical pattern. At each timestep  $t$ , the agent observes the current state  $s_t$  of the environment, which contains all the relevant information necessary for making decisions. Based on this observation, the agent selects and executes an action  $a_t$ , according to its policy  $\pi$ . This policy, which is essentially a strategy that maps states to actions, may function deterministically or probabilistically. After the action is executed, the environment transitions to a new state  $s_{t+1}$  and awards the agent with an immediate reward  $r_{t+1}$ . This reward, quantified as a numerical value, evaluates the action's efficacy in progressing towards the agent's objectives. Subsequently, the agent assimilates this feedback—comprised of both the reward and the new state—to refine its policy, employing RL algorithms designed to optimize the accumulation of long-term rewards.

*c. Deep Reinforcement learning* Deep learning, a specialized subset of machine learning, excels at identifying patterns in extensive datasets through its multi-layer neural network architecture. This approach enables computers to derive complex representations directly from raw data, leading to revolutionary advances in fields like image recognition, natural language pro-

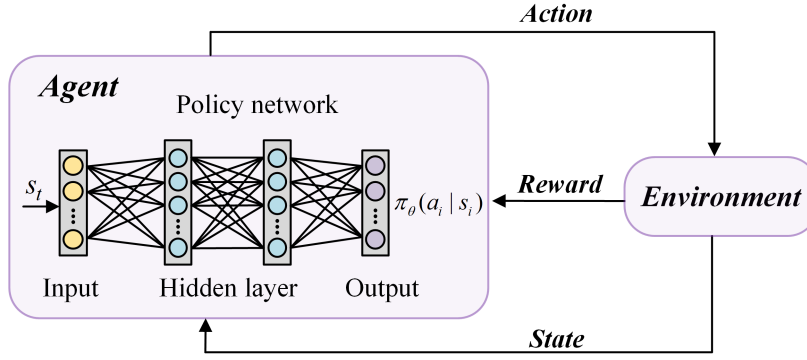


FIG. 3: DRL combines deep learning’s ability to interpret complex data with reinforcement learning’s strategy to make informed decisions.

cessing, and predictive analytics. DRL marries the potent perceptual capabilities of deep learning with the decision-making and optimization capabilities of reinforcement learning, effectively overcoming their individual limitations. Deep learning addresses the challenge of processing original, high-dimensional input data, which is problematic for traditional reinforcement learning, while reinforcement learning provides a structured decision-making framework and a goal-oriented learning mechanism that enhances the capabilities of deep learning. As depicted in Figure 3, a deep learning network transforms the intricate state of the environment into a compressed and efficient feature representation. This transformation yields a more manageable and interpretable state space for reinforcement learning algorithms. In DRL, reinforcement learning leverages these high-level features to learn and optimize decision-making policies. These policies are typically parameterized by deep neural networks, implying that the selection of actions is influenced not only by the current observation of the environmental state but also by the learned weights within the network.

### C. Proximal Policy Optimization algorithm

PPO is an advanced DRL algorithm suitable for addressing reinforcement learning challenges within both discrete and continuous action spaces. The fundamental concept of PPO revolves around enhancing performance by maximizing a surrogate objective function while ensuring the stability of policy updates. In PPO, an agent interacts with an environment to gather experience data, which is then utilized to construct the objective function. This function incorporates dominant estimates from the experience data to gauge the direction of policy improvement. During these interactions, the agent generates a sequence of trajectories ( $\tau$ ). A trajectory consists of a series of state-action pairs produced as the agent operates under the current policy, continuing until a terminal state is reached or a predetermined maximum number of steps is exceeded. Symbolically, a trajectory  $\tau$  can be represented as follows:

$$\tau = (s_0, a_0, r_1, s_1, a_1, r_2, s_2, \dots, s_{T-1}, a_{T-1}, r_T, s_T), \quad (7)$$

where,  $s_t$  represents the state at time step  $t$ ;  $a_t$  represents the action at time step  $t$ ;  $r_{t+1}$  represents the immediate reward obtained after taking action  $a_t$ ;  $T$  represents the length of the trajectory;  $s_0$  is the initial state, and  $s_T$  is the terminal state. The cumulative reward  $R(\tau)$  of a trajectory  $\tau$  is obtained by summing the rewards  $r_t$  obtained at each time step  $t$ :

$$R(\tau) = \sum_{t=0}^T r_t, \quad (8)$$

The objective function  $J(\pi_\theta)$  in the PPO algorithm aims to maximize the expected cumulative reward obtained by following the policy  $\pi_\theta$ . Mathematically, this objective function is expressed as:

$$J(\pi_\theta) = \mathbb{E}_{\tau \sim \pi_\theta} [R(\tau)], \quad (9)$$

where  $J(\pi_\theta)$  represents the expected return under policy  $\pi_\theta$ , with the expectation taken over trajectories sampled from the policy distribution  $\pi_\theta$ . The term  $R(\tau)$  denotes the total reward accumulated along a trajectory  $\tau$ . The policy gradient  $\nabla_\theta J(\pi_\theta)$ ,

indicating the direction of steepest ascent in the objective function  $J(\pi_\theta)$ , is computed using the policy gradient theorem. The gradient of the expected return is expressed as the expectation of the gradient of the log-probability of trajectories weighted by the return:

$$\nabla_\theta J(\pi_\theta) = \mathbb{E}_{\tau \sim \pi_\theta} [\nabla_\theta \log P(\tau | \theta) R(\tau)], \quad (10)$$

where  $\nabla_\theta \log P(\tau | \theta)$  represents the gradient of the log-probability of trajectories with respect to the policy parameters  $\theta$ . This computation involves sampling trajectories from the policy distribution  $\pi_\theta$  and weighting the log-probability gradients by their respective returns. The policy parameters  $\theta$  are updated iteratively using gradient ascent, with the update rule:

$$\theta_{k+1} = \theta_k + \alpha \nabla_\theta J(\pi_\theta), \quad (11)$$

where  $\theta_k$  represents the policy parameters at the  $k$ -th iteration,  $\alpha$  is the learning rate controlling the step size, and  $\nabla_\theta J(\pi_\theta)$  denotes the policy gradient.

In the PPO algorithm, the trajectories generated by the agent are instrumental in shaping the policy update process. The objective function,  $J(\pi_\theta)$ , is designed to enhance the agent's performance by maximizing the expected cumulative reward under the policy  $\pi_\theta$ . This optimization involves iteratively updating the policy parameters  $\theta$  using the policy gradient  $\nabla_\theta J(\pi_\theta)$ , while maintaining stability and preventing substantial policy shifts. The policy gradient is estimated using a collection of trajectories,  $\mathcal{D} = \{\tau_i\}_{i=1, \dots, N}$ , each generated by the agent interacting with the environment according to the policy. The policy gradient can be calculated as follows:

$$\hat{g} = \frac{1}{|\mathcal{D}|} \sum_{\tau \in \mathcal{D}} \sum_{t=0}^T \nabla_\theta \log(\pi_\theta(a_t | s_t)) R(\tau), \quad (12)$$

where  $|\mathcal{D}|$  represents the number of trajectories in  $\mathcal{D}$ , and  $T$  is the length of each trajectory. This formulation offers a simplified approach to computing the policy gradient. Moreover, PPO commonly employs a clipped surrogate objective function to facilitate more stable policy updates. This objective is expressed as:

$$L^{CLIP}(\theta) = \frac{1}{|\mathcal{D}|} \sum_{\tau \in \mathcal{D}} \sum_{t=0}^T \min(r_t(\theta)A_t, \text{clip}(r_t(\theta), 1 - \epsilon, 1 + \epsilon)A_t), \quad (13)$$

where  $r_t(\theta)$  is the likelihood ratio between the old and new policies,  $A_t$  denotes the advantage function, and  $\epsilon$  is a hyperparameter that defines the clipping range. The inclusion of this clipped surrogate objective aids in moderating the extent of policy updates, thereby stabilizing the training process.

In summary, the PPO algorithm presents a robust framework for the training of DRL agents. It operates through an iterative process of updating policy parameters aimed at maximizing the expected cumulative reward. Crucially, PPO maintains stability and mitigates the risk of substantial policy deviations. Employing policy gradients along with clipped surrogate objectives, PPO ensures effective and stable training across a diverse array of reinforcement learning tasks. This methodology not only enhances the efficiency of learning but also contributes significantly to the consistency and reliability of the training process.

#### D. DRL-Enhanced Active Flow Control

This section outlines the design of a framework utilizing DRL algorithms to address AFC problems. Firstly, it is necessary to define two fundamental elements in DRL: the agent and the environment. The agent can be designed as algorithms suitable for solving continuous action control problems, such as PPO agent or SAC agent. The CFD simulation of the flow around an elliptical cylinder is chosen as the environment for the agent to interact with. Rabault *et al.*<sup>44</sup> presented the main structure of the custom environment class, encouraging readers to delve into the detailed content. This framework design applies DRL methods to solve the AFC problem, enabling the agent to continuously learn and optimize its behavior through interaction with the environment to achieve the control goal. Fig. 4 illustrates the fundamental framework of DRL, the computational process of a single episode during training, and the formulas utilized.

- State  $s_t$ : Traditional state spaces are often too expansive for effective policy learning, requiring operations in partially observable environments. As a result, an agent's performance heavily relies on the quality and relevance of the data it can observe. The impact of partial observability of states  $s_t$  on control results was mentioned in Viquerat *et al.*<sup>31</sup>'s research. Integrating instantaneous velocity or pressure information from CFD simulations to characterize the environmental

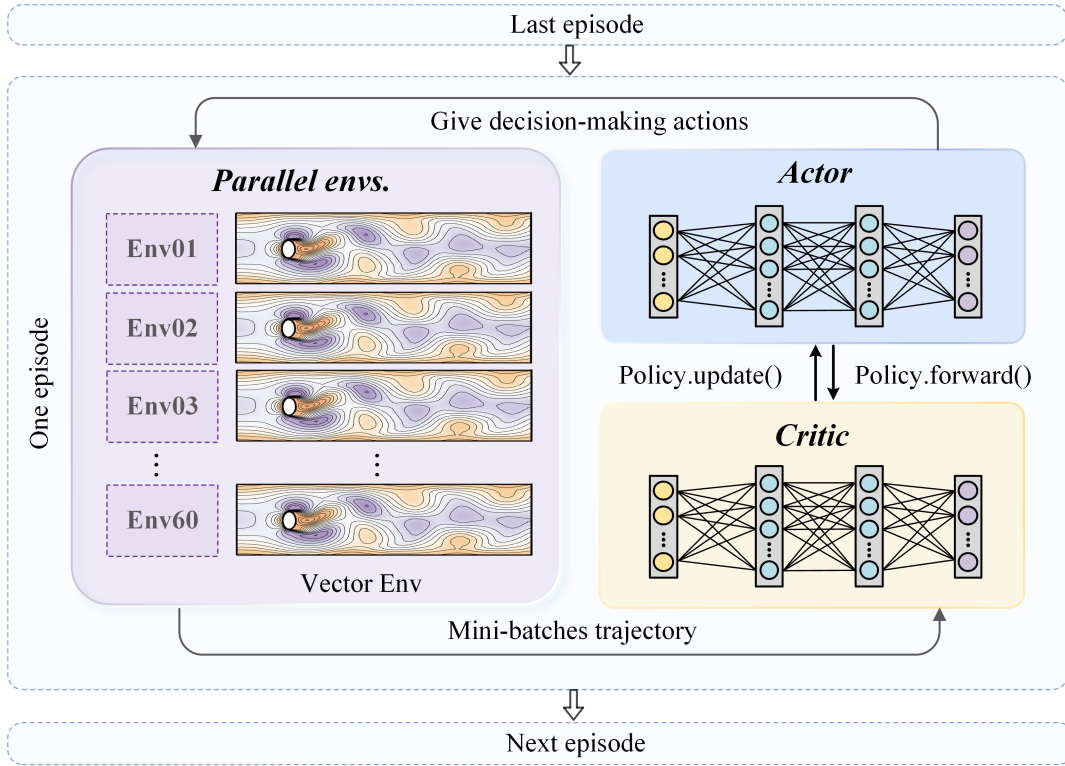


FIG. 4: DRL leverages the concurrent execution of multiple environments within a parallel computational framework. Each iteration consists of two distinct phases: exploration and optimization. During the exploration phase, the agent engages with the environment via its current policy  $\pi$ , executing actions  $a_t$ , receiving states  $s_t$  and rewards  $r_t$ , and noting terminal states. Upon the result of the iteration, the parallel computation across  $n$  environments yields a set of trajectories  $\{\tau_i\}_{i=1}^n$ , with each trajectory  $\tau_i$  comprising the sequence of states, actions, and rewards as  $\tau_i = \{(s_0, a_0), (s_1, a_1, r_1), \dots, (s_T, a_T, r_T)\}$ , where  $(s_t, a_t, r_t)$  represents the state, action, and reward at time-step  $t$ , respectively, for the  $i$ -th environment. In the optimization phase, the agent samples a minibatch of trajectories from the experience replay buffer to compute the policy gradient  $\nabla_{\theta} J(\pi_{\theta})$ . The parameters  $\theta$  of the policy network are updated using gradient ascent, i.e.,  $\theta \leftarrow \theta + \alpha \nabla_{\theta} J(\pi_{\theta})$ , where  $\alpha$  denotes the learning rate. This process iterates, with the agent deploying the updated policy  $\pi_{\theta'}$  to interact with the environment, computing the advantage function  $A(s_t, a_t)$ , and recalculating the policy gradient for subsequent updates of  $\theta$ . Through iterative refinement, the policy network incrementally enhances its action selection strategy within the environment.

state  $s_t$ , the DRL agent can effectively perceive and analyze the current flow conditions. To achieve the control objectives of reducing drag and lift around the elliptical cylinder and controlling the shedding of vortices in the wake field, multiple probes are strategically placed around the elliptical cylinder and within its wake field. This method is advantageous for gathering comprehensive data pertaining to the flow dynamics around the cylinder and subsequent wake characteristics. The design of probes placement in this study was based on the design principles articulated by Rabault *et al.*<sup>33</sup>, which advocate strategic positioning of probes around the cylinder and within the wake region of the cylinder. In their studies, Wang and Xu<sup>37</sup> and Wang *et al.*<sup>39</sup> all referred to the probes arrangement scheme proposed by Rabault *et al.*<sup>33</sup>.

- Action  $a_t$  : The control action involves the blowing and suction of two synthetic jets on the elliptical cylinder. The flow rates of the two synthetic jets are constrained such that  $Q_{\text{lower}} + Q_{\text{upper}} = 0$ . Therefore, the RL agent manipulates the velocity of the upper synthetic jets, while the lower synthetic jets has the same velocity but in the opposite direction. The velocity of the synthetic jets is set to be less than 2% of the inlet mean velocity. This restriction is imposed to prevent the agent from taking shortcuts and using excessively high jet velocities to achieve drag reduction, which contradicts the fundamental principle of AFC: energy efficiency. Furthermore, each control action lasts for 50 time steps, termed as a viscous action. Allowing faster actions could harm overall performance as they need time to influence the environment. Ensuring smooth transitions between current and updated actions is crucial. Let  $a_t$  and  $a_{t+1}$  represent the action magnitudes at consecutive time steps. To ensure a gradual transition between these actions and mitigate abrupt changes in jet velocity, a smoothing function  $S$  can be defined mathematically. The function  $S$  interpolates between the previous action magnitude  $V_{\Gamma, T_{i-1}}$  and the target action magnitude  $a$  at time step  $i$ , resulting in an updated value  $V_{\Gamma, T_i}$ . This smoothing

function can be expressed as:

$$S(V_{\Gamma_1, T_i}, a, V_{\Gamma_1, T_{i-1}}) = V_{\Gamma_1, T_i} + \beta \cdot (a - V_{\Gamma_1, T_{i-1}}), \quad (14)$$

where  $V_{\Gamma_1, T_i}$  represents the current value at time step  $i$ ,  $\beta$  is a coefficient determining the extent of adjustment towards the target action  $a$ , and  $V_{\Gamma_1, T_{i-1}}$  is the value at the previous time step  $i - 1$ . This function ensures a smooth transition between consecutive actions, with the parameter  $\beta$  controlling the smoothness of the transition.

- **Reward  $r_t$**  : This study incorporates the average drag coefficient (without control), the time-averaged value of the drag coefficient, and the time-averaged value of the lift coefficient (averaged over the duration of the action). The primary objective is to minimize the drag while maintaining a low lift coefficient; hence, the weight of the drag coefficient in the reward function is set to 1, while the lift coefficient is assigned a weight  $w$ , typically chosen to be 0.1 or 0.2. This hyperparameter  $w$  is determined through tuning. Including a constant (the average drag coefficient without control) in the reward function helps guide it towards positive rewards, which positively affects the convergence speed of the learning curve. The reward function  $f(\cdot)$  translates the drag and lift coefficients into a numerical reward assessing the agent's behavior. The specific reward function takes the following form:

$$r_{T_i} = C_{D,0} - (C_D)_{T_i} - \omega \left| (C_L)_{T_i} \right|, \quad (15)$$

$C_{D,0}$  represents the baseline drag coefficient, serving as a reference point for drag reduction.  $(C_D)_{T_i}$  denotes the drag coefficient at time step  $T_i$ , with the objective of minimizing this value relative to the baseline.  $(C_L)_{T_i}$  signifies the lift coefficient at time step  $T_i$ , whose absolute value is penalized to mitigate lift forces that may destabilize the flow around the bluff body.  $\omega$  is a weighting factor that quantifies the trade-off between minimizing drag and controlling lift fluctuations.

- **Parameter.** Time granularity in the DRL framework is crucially set based on the fluid dynamics problems studied and significantly affects agent performance and learning task complexity. Precise adjustments of this hyperparameter, informed by prior research and our ongoing strategy refinement, are vital for achieving optimized control outcomes. Each action is applied for a duration of 0.025 seconds (Corresponds to 25 numerical simulation time steps), and each episode consists of 100 control actions. The maximum total time for an episode is defined as  $T_{\max} = T_{100} = 2.5$  nondimensional time units. The shedding frequency of vortices around the elliptical cylinder in this study ranges from 0.3 to 0.4, corresponding to 6.25 to 8.33 vortex shedding cycles per episode. The length of episodes is intentionally chosen to encompass multiple shedding cycles, facilitating effective learning of the control algorithm by the agent through observation and adaptation of flow dynamics over several cycles.

## E. High-Performance Computing in DRL and CFD

The DRL training and numerical simulation in this study were conducted on a high-performance computing (HPC) system equipped with an Intel® Xeon® Platinum 8358 CPU, operating at 2.60 GHz and comprising a total of 64 cores distributed evenly across two sockets, each containing 32 cores. Numerical simulations were performed using the eighth version of the open-source software platform, OpenFOAM® version 8.<sup>46</sup> The deployment of DRL algorithms was based on the Tensorforce library.<sup>48</sup> The ANN definitions and gradient descent algorithms were facilitated using the TensorFlow open-source library.<sup>49</sup> For DRL implementation, agent was loaded using the Tensorforce platform with the PPO algorithm, and the environment was constructed using the Gym interface.<sup>50</sup> Fig. 4 illustrates the use of CFD calculations as the environment for DRL training and shows the effects of using 60 parallel CFD environments to accelerate the training process. This parallel strategy was inspired by the research of Rabault and Kuhnle<sup>51</sup> and Wang *et al.*<sup>39</sup>, and also incorporated insights from the work of Wang *et al.*<sup>39</sup> For a more comprehensive understanding, readers are encouraged to consult their works and the references therein.

## III. RESULTS

### A. Baseline Flow

*a. Vortex shedding phenomenon* Fig. 5 depicts the vortex shedding patterns within the wake field of elliptical cylinders with  $Ar$  from 0 to 2. Starting from Fig. 5(a) depicting an elliptical cylinder with  $Ar = 2$ , the wake field does not exhibit vortex shedding. This is expected as the elongated elliptical cylinder results in weak adverse pressure gradients that allow the boundary layers to stay attached for a prolonged distance. The zero vorticity contour lines in the wake extend all the way to the outlet with slight fluctuations. This suggests that the wake is largely stable, with minor flow instability due to shear in the flow. It is worth highlighting that this test case of  $Ar = 2$  serves as a special verification study for subsequent DRL control experiments. For a

stable flow field with no vortex shedding, we expect the DRL-based flow control algorithm to conform to the underlying flow physics and to not introduce any actuation since the current baseline is essentially the optimal flow configuration. To the best of our knowledge, this sanity test that verifies minimal DRL-based control is often overlooked in literature. We include this to showcase the robustness of DRL-based control across a spectrum of flow physics. We delay the discussion of DRL control to Sec. III B.

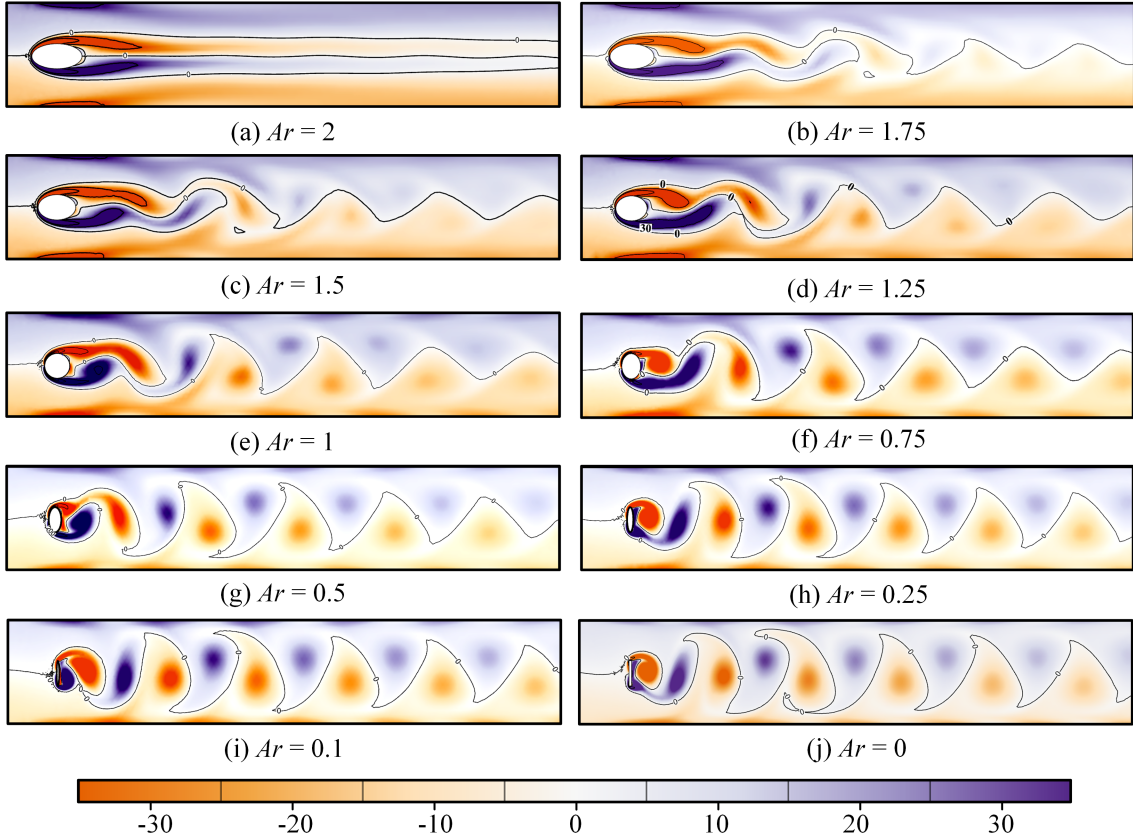


FIG. 5: Contours of instantaneous vorticity for flow around an elliptic cylinder at  $Re = 100$ , varying from  $Ar = 2$  to  $Ar = 0$ . Purple and orange indicate positive and negative vorticity, respectively. In all the depicted vorticity contours, purple represents the clockwise vortices shed from the upper side of the elliptical cylinder, while orange represents the counterclockwise vortices shed from the lower side.

As the  $Ar$  decreases to 1.75, the recirculation region behind the cylinder starts to become unstable and begins to exhibit vortex shedding phenomena. As  $Ar$  decreases further to 1.5 and 1.25, the vortices become more compact with increasing frequency, and there is increasing interaction between pairs of vortices through shearing, stretching, and detachment processes. It is also evident that the onset of vortex shedding shifts upstream with decreasing  $Ar$ . As the  $Ar$  decreases to 1, which transforms the elliptical cylinder into a perfect circle, we observe the typical von Kármán vortex street reported in many literature. This "standard aligned BvK street" is characterized by a series of regularly spaced vortices that alternately form on both sides of the cylinder. As the  $Ar$  decreases from  $Ar = 0.75$  to  $Ar = 0.25$ , the recirculation area gradually diminishes, leading to a more compact vortex structure and an increase in shedding frequency. At  $Ar = 0.1$ , for extremely low  $Ar$ , the recirculation area further decreases, resulting in an increase in both the frequency and intensity of vortex shedding. At  $Ar = 0$ , when the cylinder degenerates into a vertical flat plate, flow separates right at the two sides of the flat plate and vortex shedding becomes more pronounced. This indicates an increase in flow instability and irregularity in vortex size and shape.

Across all test cases, persistent instabilities in the form of vortices are observed at the exit of the computational domain, indicating that the fluid flow remains unstable in the downstream direction. As the fluid advances downstream, there is a tendency for the peak vortex intensity to decrease. This attenuation of vorticity is primarily attributed to the viscous diffusion effects commonly present in low Reynolds number regions. This finding is consistent with the studies by Johnson, Thompson, and Hourigan<sup>52</sup>. Between  $Ar$  of 2 and 1.25, in addition to the recirculation bubble downstream of the cylinder, two additional recirculation bubbles form near the upstream wall. As  $Ar$  is further reduced, the confined flow exhibits only one recirculation bubble. This observation is similar to that of Sahin and Owens<sup>53</sup>, where two additional recirculation bubbles appear on the solid

sidewalls of the computational domain under the influence of blockage ratio and Reynolds number. These phenomena in the wake field of elliptical cylinders represent some intriguing physical behaviors. This serves as a foundation for subsequent flow control studies.

*b. Velocity fluctuation and design of probe layout* In addition to the baseline flow field, we analyze the fluctuating component of velocity, which serves as a good indicator to inform the location of probes during control. The judicious incorporation of fluid physics knowledge within the control agents can streamline their architecture without compromising performance, as exemplified by Pastoor *et al.*<sup>54</sup>, where phase control in drag reduction of a bluff body is primarily founded upon the understanding of decoupled shear layer development and wake processes. We also utilize the physical information from the wake field to guide the flow control strategies of the agents. This aspect is particularly reflected in the practical design of the probe positions. The study by Protas and Wesfreid<sup>55</sup> elaborates on the adjustable component of the drag coefficient,  $C_D^0$ , which reflects the influence of oscillatory flow phenomena on the drag coefficient. This provides a pathway for strategic manipulation of the von Kármán vortex street to adjust the drag through targeted interventions. Building on this foundation, we tailor the physical information observed by the agents to specifically face the factors contributing to instability in the wake field.

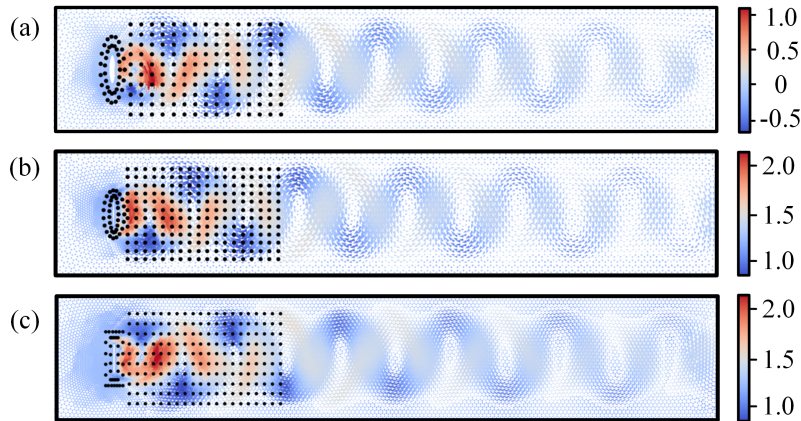


FIG. 6: The distribution of probes within the fluctuating velocity magnitude fields for different  $Ar$  : (a)  $Ar = 0.25$ ; (b)  $Ar = 0.1$ ; (c)  $Ar = 0$ .

As depicted in Fig. 6, the fluctuating magnitude velocity fields around elliptical cylinders with  $Ar$  of 0, 0.1, and 0.25 are illustrated. The positions of the black dots on the diagram represent the locations of the probes. These probes are strategically placed around the elliptical cylinder and in the downstream wake region. On one hand, the arrangement of probes around the elliptical cylinder is designed to capture physical information pertinent to the lift and drag forces, which are critical components of our control objectives. On the other hand, probes within the wake of the elliptical cylinder are positioned to encompass areas of maximum velocity fluctuations, facilitating the extraction of flow field data from regions where velocity fluctuations and vortex instabilities are most intense. The extraction of physical information from these locations enables the agents to acutely observe changes in the flow field. In Fig. 6, three tests with different  $Ar$  are shown as examples. The configurations for other  $Ar$  are fundamentally similar and are not elaborated further.

## B. Effectiveness of AFC

This section describes the performance of AFC using the DRL algorithm, which manipulates the magnitude of synthetic jets to achieve targeted flow control. At  $Re = 100$ , AFC is applied to elliptical cylinders with  $Ar$  ranging from 2 to 0, from elongated body to circular cylinder and then to a normal flat plate. The evaluation of the control's effectiveness and performance is based on several criteria: intensity of vortex shedding after control, reductions in drag coefficient, variations in lift coefficient, the actions (magnitude of the synthetic jets velocities), and the learning curves observed during the training process. Fig. 7 and Fig. 8 display the velocity magnitude snapshots of elliptical cylinders with  $Ar$  ranging from 2 to 0 under baseline and controlled conditions. More specifically, Fig. 7 shows those for  $Ar$  from 2 to 0.75, the vortices in the wake field of the controlled elliptical cylinders can be completely suppressed. In contrast, Fig. 8 illustrates those for  $Ar$  from 0.5 to 0, the vortices in the wake field of the controlled elliptical cylinders are mitigated by not fully suppressed.

Starting from Fig. 7(a) for the elliptical cylinder with  $Ar = 2$ , the baseline flow field (left) exhibits high stability with no observable vortex shedding. We applied a DRL-based flow control to this stable, non-shedding wake field, and the controlled flow field (right) behind the elliptical cylinder remained stable and nearly identical to the baseline. This sanity test indicates that the DRL-based model is consistent with flow physics and does not generate any unreasonable perturbation during the

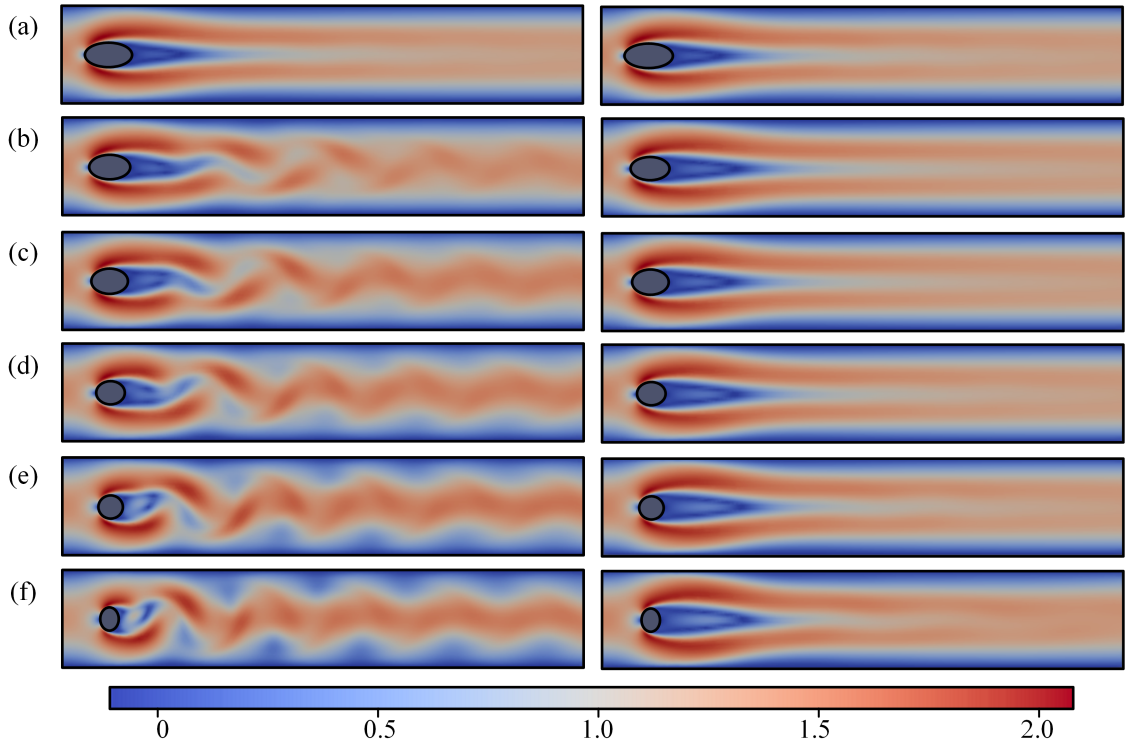


FIG. 7: Comparison of the velocity magnitude snapshots for an elliptical cylinder before and after control. Each row displays: on the left, the baseline simulation; on the right, the AFC results. (a)  $Ar = 2$ ; (b)  $Ar = 1.75$ ; (c)  $Ar = 1.5$ ; (d)  $Ar = 1.25$ ; (e)  $Ar = 1$ ; (f)  $Ar = 0.75$ .

control process. As the  $Ar$  decreases to  $Ar = 1.75$ , the application of DRL-based AFC technology successfully suppresses the vortices that originally separated alternately from both sides of the elliptical cylinder. Further reducing the  $Ar$  results in a more pronounced and frequent shedding of vortex structures in the uncontrolled wake, while the recirculation bubble downstream of the elliptical cylinder gradually decreases and becomes oscillatory. Although the flow instability gradually increases, under the conditions of  $Ar = 1.5$ ,  $1.25$ ,  $1$ , and  $0.75$ , the alternating vortex streets behind the elliptical cylinders are transformed into a stable wake field after the implementation of AFC in all cases. The DRL-based AFC technology demonstrates significant vortex shedding suppression capabilities under these conditions, highlighting the effectiveness of the AFC control strategy in enhancing the flow stability of the wake field.

In Fig. 8, as the  $Ar$  decreases to  $0.5$ ,  $0.25$ ,  $0.1$ , and  $0$ , the baseline flow becomes increasingly unstable, and the area of the recirculation region gradually decreases while the strength and frequency of vortex shedding increase. When  $Ar = 0.5$ , the frequent alternating vortex shedding is effectively suppressed after flow control is applied. The recirculation region behind the elliptical cylinder is significantly elongated, and the shedding of vortices is controlled, although the wake flow still exhibits alternating oscillations. For the controlled flow at  $Ar = 0.25$ , the recirculation bubble behind the elliptical cylinder is elongated, resembling the case at  $Ar = 0.5$ . However, there is a notable difference: the recirculation bubble now demonstrates prominent oscillations. The vortex shedding behind the cylinder continues alternately, akin to the elongated vortex structures being stretched longitudinally. Despite these instabilities, vortex shedding in the wake fields at  $Ar = 0.5$  and  $Ar = 0.25$  is reasonably mitigated compared to the baseline state. At  $Ar = 0.1$  or  $0$ , compared to baseline conditions, the recirculation bubbles behind the cylinder are elongated, and the initiation point of vortex shedding is extended further downstream. We do not observe complete suppression of vortex shedding due to the highly chaotic nature of these wake behind vertical thin bodies. Nevertheless, the vortex shedding is reduced to a lower frequency and intensity. These observations reflect the effectiveness of the control strategies in suppressing vortex shedding and stabilizing the wake field.

Fig. 9 presents a comparative analysis of the  $C_D$  and  $C_L$  before and after control intervention over  $Ar$  ranging from  $2$  to  $0.75$ . At an  $Ar$  of  $2$ , both  $C_D$  and  $C_L$  are stable, indicating that AFC does not have any effect. However, for  $Ar$  of  $1.75$ ,  $1.5$ ,  $1.25$ ,  $1$ , and  $0.75$ , upon activating synthetic jets control, there is an immediate, sharp response in  $C_D$ , which quickly descends to a value near its minimum. After half the total control duration,  $C_D$  stabilizes and remains constant at this minimal value. Similarly,  $C_L$  experiences significant fluctuations at the start of control but stabilizes near zero after half the total control duration. The reductions in  $C_D$  and  $C_L$  at different  $Ar$  are detailed in Tab. II. These observations substantiate the effectiveness of the AFC strategy underpinned by DRL algorithms. The activation of control swiftly alters the periodic behavior of both  $C_D$  and  $C_L$ ,

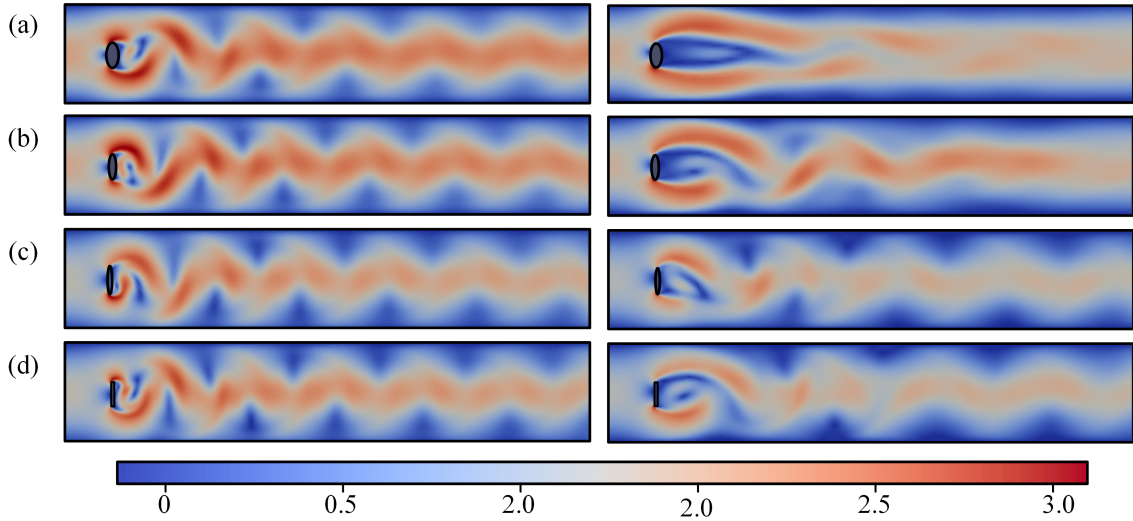


FIG. 8: Comparison of the velocity magnitude snapshots for an elliptical cylinder before and after control. Each row displays: on the left, the baseline simulation; on the right, the AFC results. (a)  $Ar = 0.5$ ; (b)  $Ar = 0.25$ ; (c)  $Ar = 0.1$ ; (d)  $Ar = 0$ .

facilitating the stabilization of  $C_D$  and  $C_L$  in the subsequent stages. This demonstrates the capability of the DRL-based AFC approach to significantly reduce the drag around an elliptical cylinder to its lowest feasible value and diminish the lift to zero.

Fig. 10 illustrates the  $C_D$  and  $C_L$  for both baseline and controlled flow conditions around an elliptical cylinder at  $Ar$  of 0.5, 0.25, 0.1, and 0. Under AFC, at  $Ar = 0.5$  and  $Ar = 0.25$ , both  $C_D$  and  $C_L$  are reduced compared to the baseline flow, yet they do not achieve the stable state observed at  $Ar = 0.75$  and higher. Initially, both the  $C_D$  and the  $C_L$  experienced abrupt changes. However, they did not fully stabilize in the subsequent period. In the latter half of the control duration,  $C_D$  and the  $C_L$  exhibited fluctuations, but both the amplitude and frequency of these fluctuations were lower than those observed in the baseline flow. At  $Ar = 0.1$  and  $Ar = 0$ , the controlled flow experiences a sharp decrease in the drag coefficient at the onset of control, followed by oscillations that persist at a lower frequency and amplitude than the baseline flow. Although complete stability is not achieved, the average value of the  $C_D$  is significantly reduced. Similarly, the  $C_L$  undergoes an initial sharp decrease and approaches near zero, then later starts to oscillate, but at a lower frequency than the baseline  $C_L$  oscillation.

Fig. 11 illustrates the time history curve of the action (the mass flow rate of synthetic jets). When performing AFC using DRL for flow around an elliptical cylinder with  $Ar$  between 0 and 2. When  $Ar = 2$ , the AFC is negligible, and the value of the action, pertaining to the control input, remains close to zero. This is a strong indication that the DRL-based model is not generating nonphysical perturbations for a stable flow field. From  $Ar = 1.75$  to  $Ar = 0.75$ , during the initial phases of control, the agent selects larger action values, corresponding to higher mass flow rates of synthetic jets. This indicates a deliberate strategy to assert flow control by introducing significant external energy inputs. As control progresses, the agent gradually diminishes the action values, thereby reducing the mass flow rate of the synthetic jets. Subsequently, in the mid to later stages, the agent's action values converge towards zero, corresponding to a near-zero mass flow rate of synthetic jets. This behavior signifies the agent's optimization towards an energy-saving state, maintaining flow characteristics with minimal control input. When  $Ar = 0.5$  and  $Ar = 0.25$ , the value of the action initially surges but does not stabilize near zero in the later stages. For  $Ar = 0.1$  and  $Ar = 0$ , the action value remains in a state of periodic fluctuation.

Overall, the results presented in Fig. 7 and Fig. 9 illustrate that the DRL-based control strategy exhibits energy efficiency and effectiveness within the range of elliptical  $Ar = 2$  to  $Ar = 0.75$ . By progressively decreasing the mass flow rate of synthetic jets, the strategy achieves flow control, reduces drag and lift forces, and does so with reduced external energy input. However, at  $Ar = 0.5$  and  $Ar = 0.25$ , the energy efficiency of the AFC strategy diminishes. At  $Ar = 0.1$  and  $Ar = 0$ , the external energy utilized by the control strategy is relatively high compared to the inlet velocity, which will be detailed in Tab. II.

In Fig. 12, we observe the learning curve during training of flow around elliptical cylinders with different  $Ar$ . At  $Ar = 2$ , the learning curve has entered the plateau phase after the initial improvement phase, indicating that the DRL training has converged. For  $Ar = 1.75$  and  $Ar = 1.5$ , the reward function initially increases from negative to positive values and then after 4,000 episodes converges near the maximum reward value. At  $Ar = 1.25$ , despite some initial fluctuations, the training reaches a relatively stable state after 3,000 episodes and eventually settles into a stable plateau. For  $Ar = 1$  and  $Ar = 0.75$ , there are significant initial fluctuations with the learning curve rising swiftly, indicating rapid progress in policy learning. After 2,000 episodes, the training demonstrates a stable convergence trend, with minor fluctuations in the reward value between 2,000 and 5,000 episodes. This shows that the PPO algorithm has successfully learned an effective strategy, exhibiting commendable convergence and stability in performance. At  $Ar = 0.5$ , the speed of training convergence begins to slow, trending towards convergence after 4,000

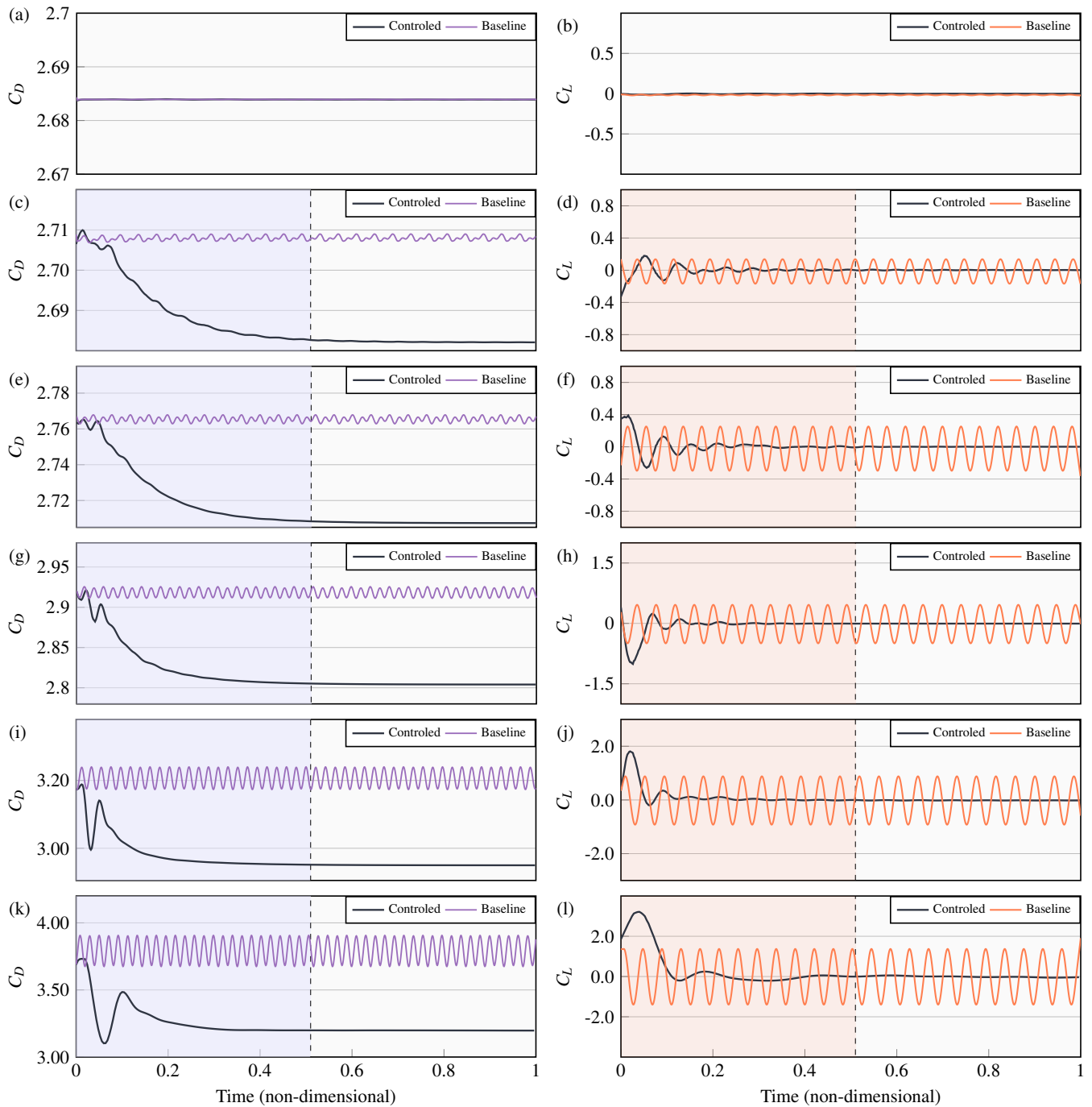


FIG. 9: Comparison of  $C_D$  and  $C_L$  before and after control. The background color represents the unstable stage of control, and the absence of background color means that the corresponding drag or lift has been in a stable stage during this period. (a) and (b)  $Ar = 2$ ; (c) and (d)  $Ar = 1.75$ ; (e) and (f)  $Ar = 1.5$ ; (g) and (h)  $Ar = 1.25$ ; (i) and (j)  $Ar = 1$ ; (k) and (l)  $Ar = 0.75$ .

episodes, with the reward values stabilizing between 4,000 and 10,000 episodes. At  $Ar = 0.25$ , training approaches convergence after 8,000 episodes, reaching a total of 20,000 episodes, with a mid-to-late plateau marking stable convergence. At  $Ar = 0.1$  and  $Ar = 0$ , the training convergence is extremely slow, with signs of convergence only appearing after nearly 12,000 episodes.

The DRL algorithm exhibits rapid initial convergence and reaches a stable plateau during the mid-to-late stages for  $Ar = 1.25$ , 1 and 0.75, showcasing excellent convergence and stability throughout the training process. Training also achieves stable convergence within 5,000 episodes for  $Ar = 1.5$  and  $Ar = 1.75$ . However, for  $Ar = 0.5$ , 0.25, 0.1 and 0, as the flow phenomena

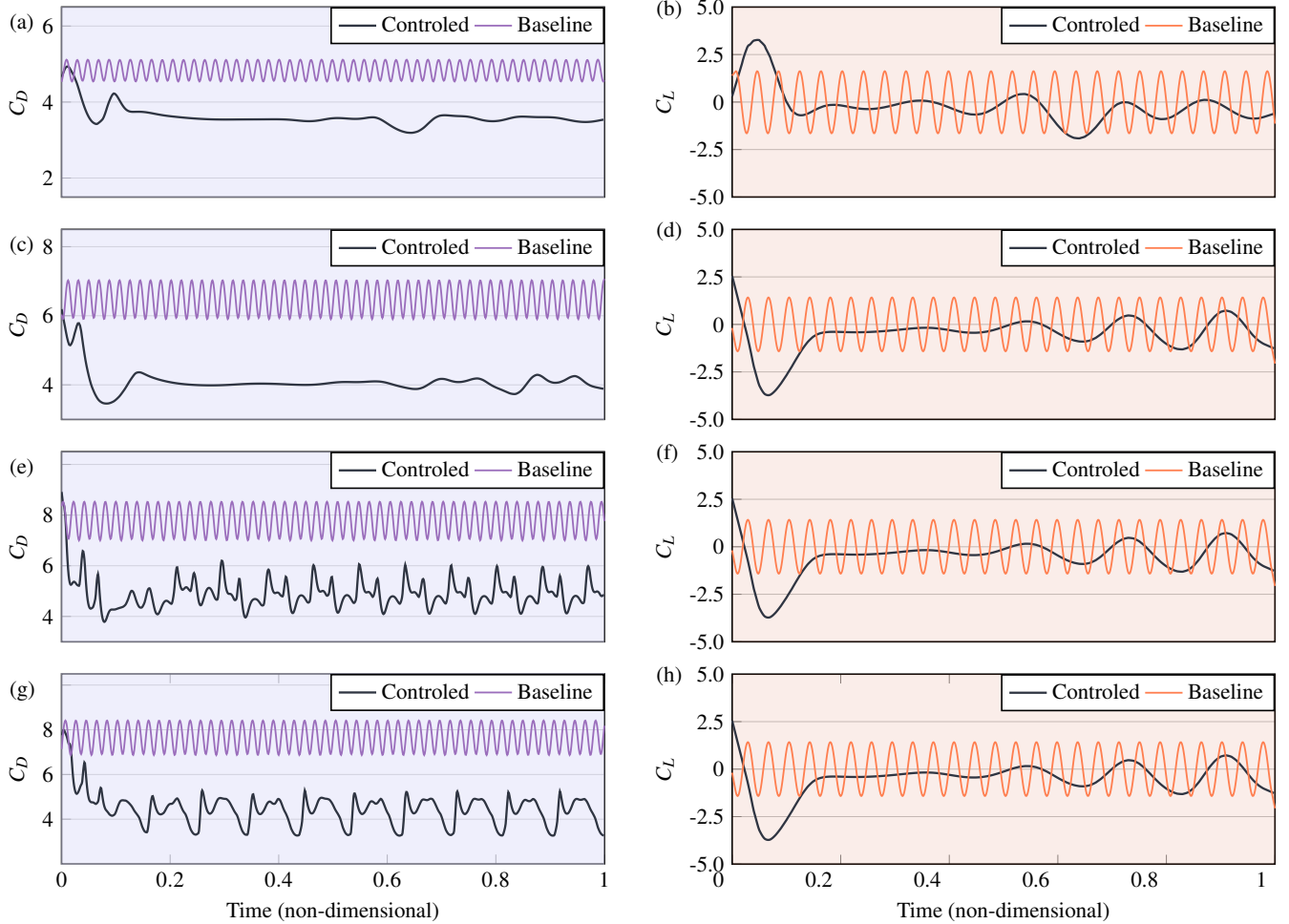


FIG. 10: Comparison of  $C_D$  and  $C_L$  before and after control. The background color indicates that the drag or lift coefficient is still in an unstable stage after flow control. (a)  $Ar = 0.5$ ; (b)  $Ar = 0.25$ ; (c)  $Ar = 0.1$ ; (d)  $Ar = 0$ .

become increasingly complex, the control challenge intensifies, leading to a noticeable slowdown in convergence speed. This indicates that for flow scenarios with higher degrees of instability, the convergence performance of DRL training is compromised, requiring a larger number of training iterations to reach stable convergence.

Tab. II presents the effectiveness of AFC techniques based on DRL algorithms, targeting elliptical cylinders with  $Ar$  ranging from 0 to 2. It meticulously details the values of  $C_D$  and  $C_L$  before and after the application of control, along with their respective rates of change. Additionally, it describes the magnitude of the mass flow rate of the synthetic jets utilized for control and its ratio relative to the inflow rate. When the  $Ar$  is set to 2, the baseline flow has reached a steady state. During the application of flow control, the agent does not use external energy to disrupt this stable flow field, which demonstrates the intelligence of the DRL-based AFC. This reflects the adaptability and intelligent decision-making of AFC control in maintaining flow stability. For elliptical cylinders with  $Ar$  of 1.75, 1.5, 1.25, 1, and 0.75, the  $C_D$  reduction rates are 0.9%, 2.1%, 3.9%, 8.0%, and 15.7% respectively, while the  $C_L$  reduction rates exceed 95% in each case. These results highlight the efficacy of the DRL-based AFC technology in effectively suppressing both  $C_D$  and  $C_L$  within the  $Ar$  range of 1.75 to 0.75, demonstrating the efficiency of the DRL-based intelligent control strategy. However, as  $Ar$  decreases to 0.5, 0.25, 0.1, and 0, even though the  $C_D$  reduction rates significantly increase to 26.9%, 35.9%, 37.6%, and 43.6%, the  $C_L$  reduction rates are 68.0%, 66.1%, 50.2%, and 60.0% respectively. This indicates that while the DRL-based control strategy achieves significant reductions in  $C_D$ , its effect on suppressing  $C_L$  is limited and does not completely eliminate  $C_L$  around the elliptical cylinder. As the  $Ar$  further decreases, the AFC technique based on the DRL algorithm does not fully suppress vortex shedding behind the elliptical cylinder, but merely delays the shedding process. The reduction in  $C_L$  coefficients aligns with the flow snapshots presented in Fig. 8, showing that vortex shedding still occurs, albeit with controlled frequency and intensity. These phenomena suggest that at very low  $Ar$  values, the control strategy faces challenges in managing more complex and unstable flow conditions.

On the other hand, the action performed by the agent is defined as the value of the mass flow rate of the synthetic jets. The

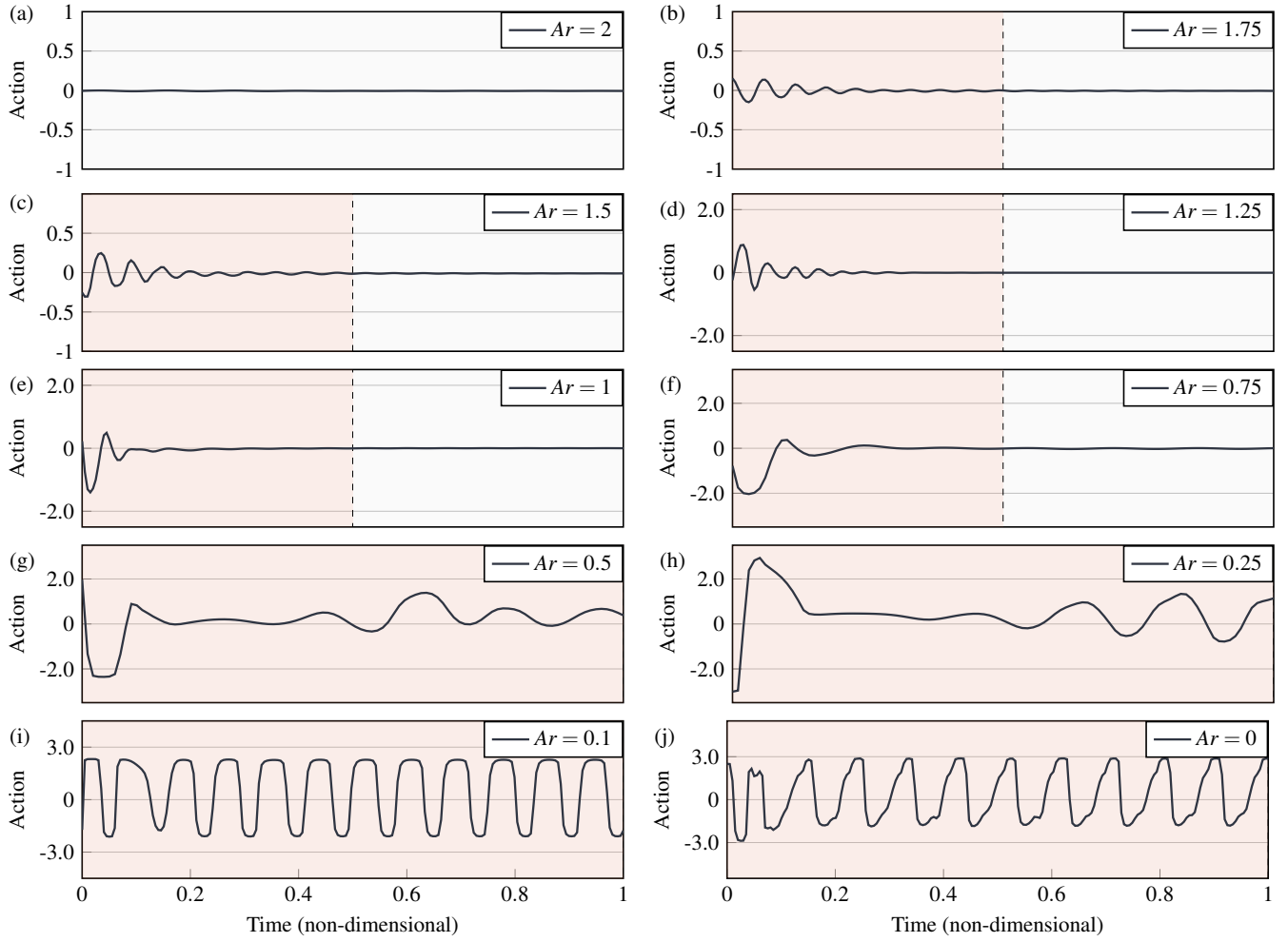


FIG. 11: Action, which is the mass flow rate of the synthetic jets. The background color represents that the value of the action is in an unstable stage, and the absence of a background color means that the action has been in a stable stage during this period. (a)  $Ar = 2$ ; (b)  $Ar = 1.75$ ; (c)  $Ar = 1.5$ ; (d)  $Ar = 1.25$ ; (e)  $Ar = 1$ . (f)  $Ar = 0.75$ ; (g)  $Ar = 0.5$ ; (h)  $Ar = 0.25$ ; (i)  $Ar = 0.1$ ; (j)  $Ar = 0$ .

TABLE II: The control effect of elliptical cylinder under DRL-based AFC.

$Ar$	$Re$	$\bar{C}_{D,Baseline}$	$\bar{C}_{D,Controlled}$	Drag Reduction (%)	$\bar{C}_{L,Baseline}$	$\bar{C}_{L,Controlled}$	Lift Reduction (%)	$\bar{a}$	$\bar{a}$ ratio (%)
2	100	2.684	2.684	0.0	0.016	0.016	0	0	0
1.75	100	2.707	2.684	0.9	0.165	0.001	99.7	0.007	0.7
1.5	100	2.765	2.707	2.1	0.302	0.002	99.4	0.009	0.9
1.25	100	2.918	2.804	3.9	0.541	0.006	98.9	0.006	0.6
1	100	3.207	2.951	8.0	1.022	0.011	98.9	0.001	0.1
0.75	100	3.792	3.197	15.7	1.603	0.076	95.2	0.010	1.0
0.5	100	4.837	3.533	26.9	1.937	0.619	68.0	0.049	4.9
0.25	100	6.503	4.167	35.9	1.707	0.579	66.1	0.126	12.6
0.1	100	7.812	4.876	37.6	1.196	0.596	50.2	0.499	49.9
0	100	7.679	4.331	43.6	1.513	0.605	60.0	0.521	52.1

a.  $\bar{C}_{D,Baseline}$  and  $\bar{C}_{L,Baseline}$  represents the time-averaged drag coefficient of the elliptical cylinder once the baseline flow has fully developed.

b.  $\bar{C}_{D,Controlled}$ ,  $\bar{C}_{L,Controlled}$ , and  $\bar{a}$  denote the time-averaged values under stable conditions after AFC is applied, excluding the transient response phase.

c.  $\bar{a}$  ratio (%) represents the ratio of the mass flow rate of the synthetic jets to the flow rate from the inlet.

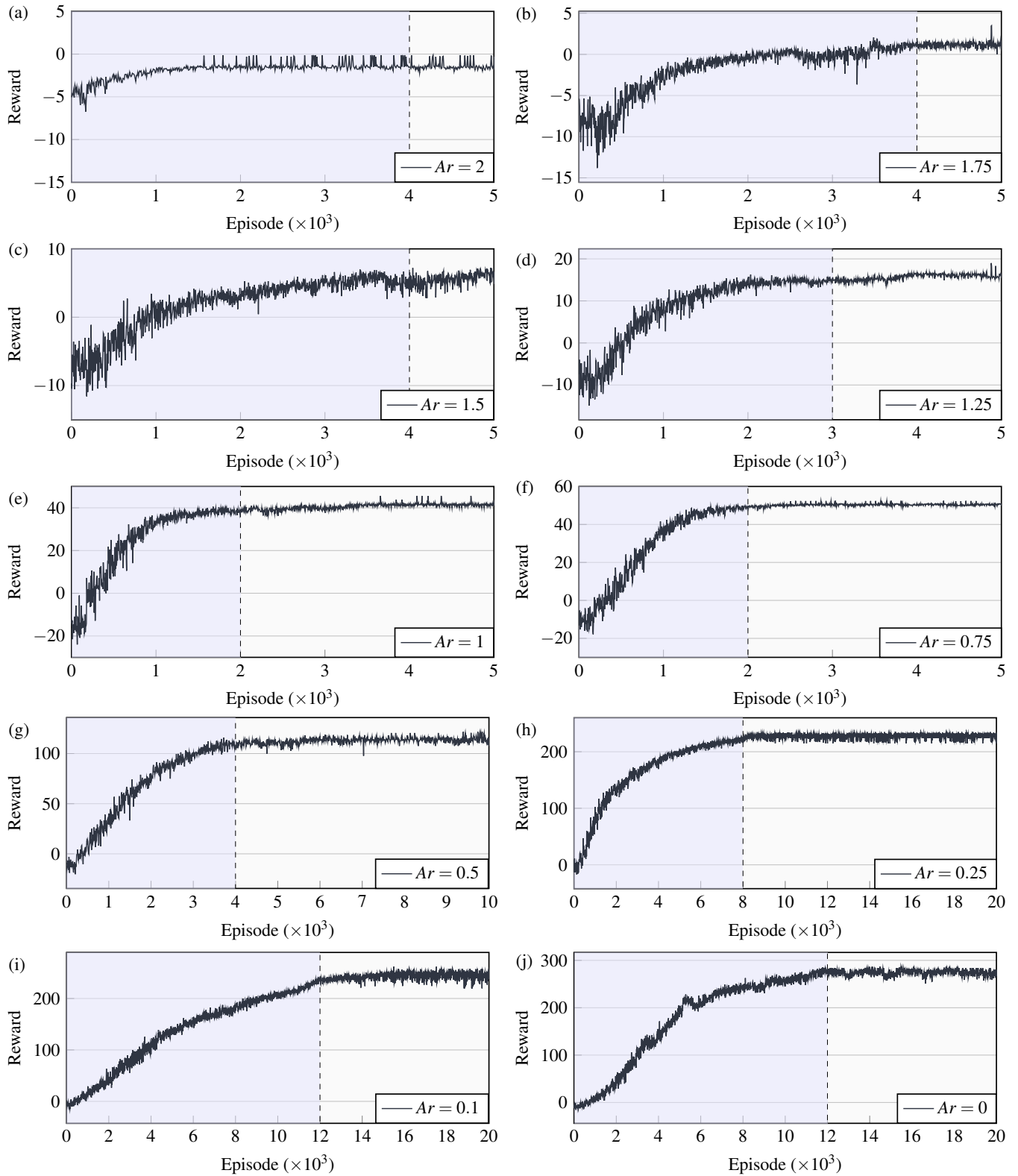


FIG. 12: When  $Ar$  of the elliptical cylinder is in the range of 2-0, the learning curve of PPO algorithm training. (a)  $Ar = 2$ ; (b)  $Ar = 1.75$ ; (c)  $Ar = 1.5$ ; (d)  $Ar = 1.25$ ; (e)  $Ar = 1$ . (f)  $Ar = 0.75$ ; (g)  $Ar = 0.5$ ; (h)  $Ar = 0.25$ ; (i)  $Ar = 0.1$ ; (j)  $Ar = 0$ .

mass flow rates of the jets are normalized as  $Q_i^* = Q_i/Q_c$ , where  $Q_c = \int_{-R}^R \rho U(y) dy$  represents the mass flow rate contributed by the inlet parabolic profile intersecting the diameter of the elliptical cylinder. Consequently,  $Q_i^*$  signifies the relative intensity of the control jets in relation to the incoming flow. For  $Ar$  greater than 0.75, the ratio of synthetic jets to the inflow is less than 1%, indicating that the mass flow rate used in the flow control strategy proposed by the PPO agent is very minimal. This aligns with the energy efficiency requirements of AFC technologies. At  $Ar$  values of 0.75, 1, 1.25, 1.5, and 1.75, the elliptical cylinder achieves  $C_D$  reduction, simultaneously attenuating up to 95% of  $C_L$  with very low energy consumption from external excitation. When  $Ar$  equals 0.5, 0.25, and 0.1, the ratio of synthetic jets to the inflow significantly increases. Despite this, the capability to attenuate  $C_L$  decreases. At lower  $Ar$  values, despite employing higher energy from external excitation, the instability in the wake field cannot be fully controlled.

In their research, Protas and Wesfreid<sup>55</sup> elucidated that the drag coefficient consists of two components: (i) the invariant drag ( $C_D^b$ ), which remains constant at a given Reynolds number; and (ii) the amendable drag correction ( $C_D^0$ ), associated with oscillatory flow phenomena within the fluid, representing the additional resistance arising from fluid oscillations or fluctuations. This portion of drag can be adjusted through external interventions, indicating the influence of unstable flow regions and the potential for control. In our research, the flow field is controlled by utilizing external excitation, such as synthetic jets, to mitigate the additional resistance caused by instability, thereby optimizing the overall fluid dynamic performance. As the  $Ar$  of the elliptical cylinder decreases, the pulsations, oscillations, and instabilities within the wake intensify, thereby enhancing the controllable component of the drag. This is the reason why the drag reduction rate gradually increases as  $Ar$  decreases in Tab. II.

The control strategies derived from DRL-based AFC technology exhibit greater complexity compared to conventional harmonic forcing implemented in previous works (Bergmann, Cordier, and Brancher<sup>56</sup>), highlighting the value of employing ANN as controllers. Typically, approximately 93% of the drag induced by the shedding of vortices is suppressed by the discovered control laws, with minimal jet intensities required for drag reduction. In our research, the control strategy derived from the DRL-based AFC system dynamically responds in real time to variations in the flow state. This emphasizes its capability to adaptively adjust to changing conditions, demonstrating the robustness and responsiveness of the AFC framework. Furthermore, for elliptical cylinders with  $Ar$  of 1.75, 1.5, 1.25, 1, and 0.75, the magnitude of the mass flow rate injected by the jets normalized by the mass flow rate of the mainstream intersecting with the cylinder is within 1%.

### C. Analysis of the Controlled Flow

Fig. 13 illustrates the suppression of vortex shedding in the wake of elliptical cylinders under the influence of AFC based on DRL. The elliptical cylinders examined have  $Ar$  of 2, 1.75, 1.5, 1.25, 1.0, and 0.75, scenarios in which vortex shedding can be completely suppressed. At the initial moment of control ( $T_1$ ), vortices in the wake of the elliptical cylinders are fully developed. During this phase, vortices are observed detaching from the cylinder at a consistent frequency and intensity, forming a Kármán vortex street in the downstream flow. As the control process advances ( $T_2$ ), external excitation methods, such as synthetic jets, are introduced to suppress the vortices in the wake of the elliptical cylinders. The objective of the control is to alter the characteristics of the flow field to weaken or eliminate the formation and persistence of vortices. With the progression of the control measures, a snapshot of the flow field is captured at the result of the control ( $T_3$ ). At this juncture, vortices within the wake of the elliptical cylinders are observed to be suppressed, demonstrating the effectiveness of the DRL-based AFC strategy in stabilizing complex fluid dynamics.

In the study of elliptical cylinders, the phenomenon of vortex shedding and its control are crucial for understanding the structure of flow fields. For elliptical cylinders with different  $Ar$ , the behavior of the flow fields shows significant differences. At  $Ar = 2$ , both before and after control, the instantaneous vorticity maps at moments  $T_1$ ,  $T_2$ , and  $T_3$  demonstrate a high degree of stability in the flow field, with no evident vortex shedding observed. For elliptical cylinders with  $Ar$  values of 1.75, 1.5, and 1.25, at  $T_1$ , alternating vortices form behind the cylinder, influenced by the elliptical shape effect, which results in lower intensity and frequency of vortex shedding. By  $T_2$ , with the initiation of control, synthetic jets quickly intervene in the regular vortex shedding process, leading to a delay in vortex detachment and the formation of "elongated vortex structures." The original vortices are significantly elongated and narrowed, and the instantaneous recirculation bubbles are also elongated longitudinally and tend towards stability. By  $T_3$ , the original vortex shedding has been completely suppressed, with no new vortices forming, and the instantaneous recirculation bubbles reach their maximum extent and remain stable, demonstrating the effectiveness of the control strategy.

At  $Ar = 1$  and 0.75, during the  $T_1$  phase, a standard Bénard–von Kármán vortex street forms behind the elliptical cylinder, characterized by a series of regularly spaced vortices. These vortices alternately shed from both sides of the cylinder, creating a regular pattern of vortex arrangement. Moving into the second phase ( $T_2$ ), similar to cases with higher aspect ratios ( $Ar = 1.75, 1.5, 1.25$ ), the recirculation bubbles behind the cylinder are elongated longitudinally, and the originally shed vortices are also elongated and narrowed, with shearing interactions occurring between them. By the third time point ( $T_3$ ), the vortices behind the elliptical cylinder are completely suppressed, and the regions of positive and negative vorticity in the flow field nearly achieve symmetry, demonstrating high stability.

Fig. 14 delineates scenarios where the suppression of vortex shedding from elliptical cylinders is not entirely effective for  $Ar$

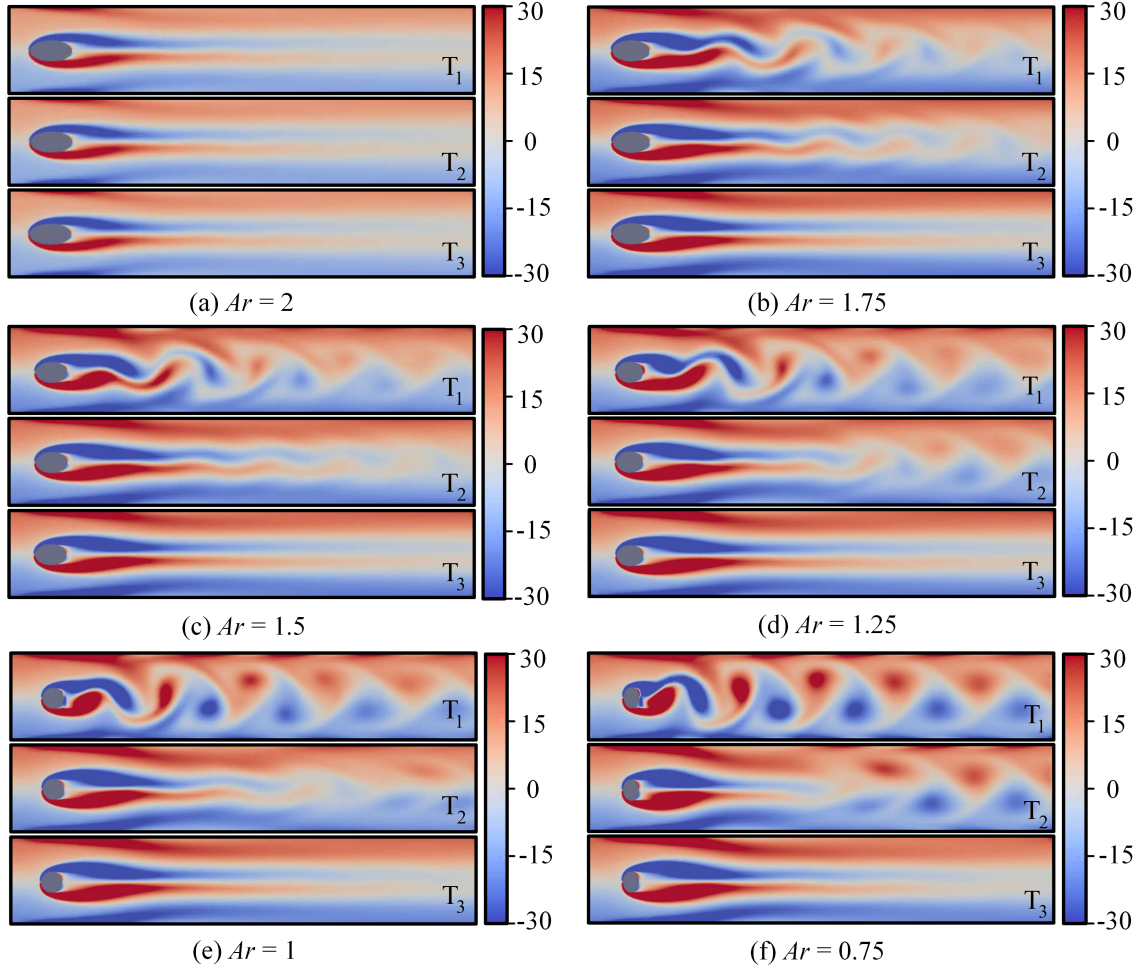


FIG. 13: When  $Ar = 2, 1.75, 1.5, 1.25, 1, 0.75$ , the vortex shedding of the elliptical cylinder can be completely suppressed. The streamwise snapshots of the wake flow field behind an elliptical cylinder, where the vortex shedding process is suppressed, feature key moments designated as  $T_1$ ,  $T_2$ , and  $T_3$ . These represent the instances of the onset of control (when the vortex is fully developed), during the control process, and at the result of control, respectively.

of 0.5, 0.25, 0.1, and 0. At  $T_1$ , the vortex shedding behind the cylinder is fully developed,  $T_2$  represents the control phase, and  $T_3$  provides a snapshot of the flow field after control cessation. For  $Ar = 0.5$  and  $Ar = 0.25$ , During the  $T_1$  phase, vortices are observed detaching from the cylinder with certain frequency and intensity, forming a Kármán vortex street in the downstream wake. In the  $T_2$  phase, as control commences, the recirculation bubble is noted to elongate longitudinally to some extent, with the recirculation area appearing relatively symmetric and stable. The intervention of synthetic jets delays the detachment of vortices, which are stretched and deformed due to shear with the side walls. By  $T_3$ , the initially generated vortices are significantly elongated and deformed, exiting the computational domain, yet the recirculation bubble behind the cylinder remains unstable and continues to oscillate, leading to new vortex shedding. The emergence of new irregular vortex shedding highlights persistent instability behind the elliptical cylinder. For elliptical cylinders with  $Ar = 0.5$  and  $Ar = 0.25$ , the DRL-based control strategy does not completely suppress vortex shedding. The instability of the wake field is mitigated, demonstrating partial efficacy of the control strategy in manipulating flow dynamics, although full stability is not achieved.

For  $Ar = 0.1$  and  $Ar = 0$ , during  $T_1$ , the vortex shedding frequency and intensity from the cylinder are more severe compared to  $Ar = 0.5$ , with enhanced flow instability. Multi-level vortex shedding occurs, with primary and secondary vortices differing in shape, frequency, and intensity. At  $T_2$ , vortices behind the cylinder are elongated and delayed, and the recirculation area significantly enlarges. The instability of the recirculation area manifests as asymmetry, swinging, and oscillation phenomena. By  $T_3$ , although the original shedding vortices are elongated and expelled from the computational domain, new, unstable, and irregular shedding occurs. Shed vortices swinging to the side walls are sheared, stretched, and undergo deformation, resulting in irregularly shaped vortices. This highlights the persistent challenges in managing flow dynamics and instability at lower  $Ar$ .

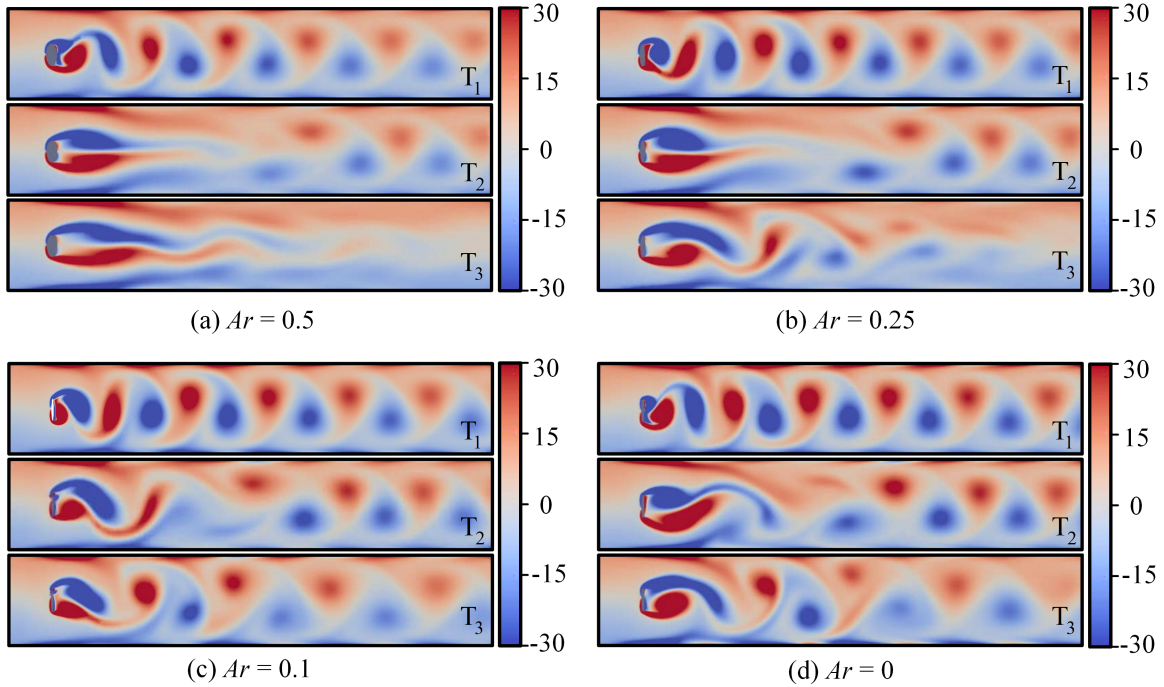


FIG. 14: When  $Ar = 0.5, 0.25, 0.1$  and  $0$ , vortex shedding from the elliptical cylinder is not entirely suppressed. The streamwise snapshots of the wake flow field behind the elliptical cylinder capture key moments designated as  $T_1, T_2,$  and  $T_3$ . These correspond to the initiation of control (when the vortex is fully developed), the early phase of the control process, the mid-to-late phase of the control process, and the termination phase of control, respectively.

#### IV. CONCLUSIONS

In this study, we investigate the use of DRL-based AFC to suppress vortex shedding, reduce drag, and mitigate lift fluctuations of elliptical cylinders at a Reynolds number of 100. The  $Ar$  of the elliptical cylinder ranges from an ellipse ( $Ar = 2.0$ ) to a circle ( $Ar = 1.0$ ), and finally to a flat plate ( $Ar = 0$ ). We employ the PPO algorithm to precisely control the mass flow rates of synthetic jets located on the upper and lower surfaces of the elliptical cylinder. The primary objective of this work is to gain further insights into the control capabilities of DRL algorithms for complex flow systems. The main findings of this study can be summarized as follows:

- At  $Ar = 2$ , the baseline flow is already in a stable state. When AFC is applied, the agent does not perform any actions that would disturb the flow field. This indicates that the DRL agent is capable of recognizing a stable flow condition and making intelligent decisions accordingly. However, for  $Ar$  of 1.75, 1.5, 1.25, 1, and 0.75, the reduction rates in the drag coefficient around the cylinder are respectively 0.9%, 2.1%, 3.9%, 8.0%, and 15.7%, while the reduction rates in lift coefficient are 99.7%, 99.4%, 98.9%, 98.9%, and 95.2%. These data indicate that the AFC strategy based on DRL is capable of significantly minimizing the periodically fluctuating drag coefficient to minimal values and stabilizing it, while also maintaining the oscillating lift coefficient near zero. This demonstrates the efficacy of DRL in AFC applications, effectively reducing the lift and drag around elliptical cylinder with  $Ar$  ranging from 0.75 to 1.75. Visualizations of velocity fields reveal that the original periodically shedding vortices transition to stable flow fields with no vortex shedding after flow control. Instantaneous vorticity maps during the control process show that with the activation of synthetic jets, the vortices downstream of the elliptical cylinder are progressively elongated. The originally unstable recirculation area behind the cylinder transforms into a stable, symmetrical recirculation bubble, ceasing the production of new vortices. These results underscore the robust adaptability of DRL-based AFC across different elliptical cylinder shapes ( $Ar$  between 0.75 and 1.75), and its capability of learning optimal control strategies directly through interaction with the environment to achieve a reduction in drag and lift coefficients around the cylinder. Moreover, for elliptical cylinders with  $Ar$  of 1.75, 1.5, 1.25, 1, and 0.75, the mass flow rate ratios of synthetic jets relative to the inlet flow rate are 0.7%, 0.9%, 0.6%, 0.1%, and 1.0% respectively. This underscores that the flow control strategy efficiently utilizes less than 1% of external excitation energy, exemplifying its energy-saving capability for effective flow control.
- When the  $Ar$  of the elliptical cylinder decreases to 0.5, 0.25, 0.1, and 0, the reduction rates of the drag coefficient and lift

coefficient are 26.9%, 35.9%, 37.6%, and 43.6%, respectively, while the corresponding reduction rates for the lift coefficient are 68.0%, 66.1%, 50.2%, and 60.1%. Despite the effective reduction in both drag and lift coefficients achieved by the DRL-based AFC strategy, vortex shedding phenomena have not yet stabilized compared to cases with larger  $Ar$  values. The initial phase of control exhibits distinct fluctuations, followed by low-frequency and low-amplitude oscillations in the drag and lift coefficients, which are lower than the baseline. Particularly, for  $Ar$  values of 0.1 and 0, the drag and lift coefficients experience a sharp decrease initially, followed by moderate-amplitude, low-frequency periodic oscillations. This indicates that for elliptical cylinders with  $Ar$  ranging from 0.5 to 0, the AFC control strategy can partially suppress lift and reduce drag. From the vorticity plots of the control process, for  $Ar$  values of 0.5 and 0.25, the recirculation region behind the elliptical cylinder is elongated during the initial phase of control, with symmetric recirculation bubbles. As the control progresses, the recirculation region becomes unstable, exhibiting lateral oscillations and the shedding of long, narrow vortices. Similarly, for  $Ar$  values of 0.1 and 0, the recirculation region undergoes elongation during the control phase, with high-frequency and large-amplitude oscillations, accompanied by the shedding of new vortices. After a significant period of control, the shedding of vortices is somewhat alleviated, with a decrease in both the frequency and intensity of vortex shedding. Correspondingly, for elliptical cylinders with  $Ar$  values of 0.5, 0.25, 0.1, and 0, the ratios of the mass flow rates of the synthetic jets relative to the incoming flow rate are 4.9%, 12.6%, 49.9%, and 52.1%, respectively. This suggests that despite the use of higher external energy, the lift coefficient cannot be completely controlled to prevent oscillations and fluctuations.

In conclusion, for elliptical cylinders with  $Ar$  ranging from 1.75 to 0.75, intelligent agents trained using the PPO algorithm have adeptly learned to adopt an energy-efficient flow control strategy. The control policies based on the PPO algorithm significantly reduce lift around the elliptical cylinder, greatly diminish drag, and completely suppress vortex shedding in the wake. Regarding elliptical cylinder with  $Ar$  values ranging from 0.5 to 0, the control strategies obtained from agents trained with the PPO algorithm can moderately alleviate vortex shedding and reduce the amplitude and frequency of fluctuations in lift and drag coefficients. These control results demonstrate the adaptability of DRL-based AFC strategies to various geometric shapes, their robustness against uncertainties, and their ability to handle complex problems. This makes DRL-based AFC particularly suitable for controlling complex fluid dynamic systems.

## ACKNOWLEDGMENTS

The authors would like to express their gratitude to Dr. Jean Rabault (University of Oslo, Oslo, Norway), Dr. Jichao Li (National University of Singapore, Singapore), and Mr. Qiulei Wang (The University of Hong Kong, Hong Kong SAR, China) for making their open-source codes for DRL and numerical simulation available online. These resources have significantly contributed to the research presented in this paper. The relevant code repositories can be accessed at <https://github.com/jerabaul29/Cylinder2DFlowControlDRLParallel><sup>33,57</sup>, [https://github.com/npuljc/RL\\_control\\_Nek5000](https://github.com/npuljc/RL_control_Nek5000)<sup>38,58</sup>, and <https://github.com/venturi123/DRLinFluids><sup>39,59</sup>.

## AUTHOR DECLARATIONS

### A. Conflict of Interest

The authors report no conflict of interest.

### B. Author Contributions

**Wang Jia:** Conceptualization (equal); Data curation (lead); Formal analysis (lead); Methodology(lead); Validation (lead); Visualization (lead); Writing – original draft (lead). **Hang Xu:** Conceptualization (equal); Investigation (equal); Supervision (lead); Validation (equal); Writing –review & editing (lead).

## DATA AVAILABILITY

The data that support the findings of this study are available from the corresponding author upon reasonable request.

## AUTHOR ORCIDS

Wang Jia <https://orcid.org/0009-0008-2786-397X>

Hang Xu <https://orcid.org/0000-0003-4176-0738>.

## REFERENCES

- <sup>1</sup>S. S. Collis and R. D. Joslin, "Issues in active flow control: theory, control, simulation, and experiment," *Progress in aerospace sciences* **40**, 237–289 (2004).
- <sup>2</sup>M. Jahanmiri, "Active flow control: a review," *Flow Measurement and Instrumentation* **21**, 7–28 (2010).
- <sup>3</sup>A. Awada, R. Younes, and A. Ilinca, "Review of vibration control methods for wind turbines," *Energies* **14** (2021), 10.3390/en14113058.
- <sup>4</sup>L. Wang, R. Hu, L. Li, and S. Fu, "Detached-eddy simulations for active flow control," *AIAA Journal* **56**, 1447–1462 (2018).
- <sup>5</sup>S. Aram, Y.-T. Lee, H. Shan, and A. Vargas, "Computational fluid dynamic analysis of fluidic actuator for active flow control applications," *AIAA Journal* **56**, 111–120 (2018).
- <sup>6</sup>R. Jain, H. Yeo, and I. Chopra, "Computational fluid dynamics—computational structural dynamics analysis of active control of helicopter rotor for performance improvement," *Journal of the American Helicopter Society* **55**, 42004 (2010).
- <sup>7</sup>Y. Li, J. Chang, C. Kong, and W. Bao, "Recent progress of machine learning in flow modeling and active flow control," *Chinese Journal of Aeronautics* **35**, 14–44 (2022).
- <sup>8</sup>J. Pozorski and M. Waclawczyk, "Mixing in turbulent flows: An overview of physics and modelling," *Processes* **8** (2020), 10.3390/pr8111379.
- <sup>9</sup>M. Reichstein, G. Camps-Valls, B. Stevens, M. Jung, J. Denzler, N. Carvalhais, and Prabhat, "Deep learning and process understanding for data-driven earth system science," *Nature* **566**, 195–204 (2019).
- <sup>10</sup>S. Subramaniam, "Multiphase flows: Rich physics, challenging theory, and big simulations," *Phys. Rev. Fluids* **5**, 110520 (2020).
- <sup>11</sup>S. L. Brunton, B. R. Noack, and P. Koumoutsakos, "Machine learning for fluid mechanics," *Annual Review of Fluid Mechanics* **52**, 477–508 (2020).
- <sup>12</sup>S. L. Brunton and B. R. Noack, "Closed-Loop Turbulence Control: Progress and Challenges," *Applied Mechanics Reviews* **67**, 050801 (2015).
- <sup>13</sup>F. Ren, H.-b. Hu, and H. Tang, "Active flow control using machine learning: A brief review," *Journal of Hydrodynamics* **32**, 247–253 (2020).
- <sup>14</sup>K. Arulkumaran, M. P. Deisenroth, M. Brundage, and A. A. Bharath, "Deep reinforcement learning: A brief survey," *IEEE Signal Processing Magazine* **34**, 26–38 (2017).
- <sup>15</sup>V. François-Lavet, P. Henderson, R. Islam, M. G. Bellemare, J. Pineau, *et al.*, "An introduction to deep reinforcement learning," *Foundations and Trends® in Machine Learning* **11**, 219–354 (2018).
- <sup>16</sup>H. Wang, N. Liu, Y. Zhang, *et al.*, "Deep reinforcement learning: a survey," *Frontiers of Information Technology & Electronic Engineering* **21**, 1726–1744 (2020).
- <sup>17</sup>C. Janiesch, P. Zschech, and K. Heinrich, "Machine learning and deep learning," *Electronic Markets* **31**, 685–695 (2021).
- <sup>18</sup>Y. LeCun, Y. Bengio, and G. Hinton, "Deep learning," *Nature* **521**, 436–444 (2015).
- <sup>19</sup>A. Dargazany, "Drl: Deep reinforcement learning for intelligent robot control – concept, literature, and future," (2021), arXiv:2105.13806 [cs.RO].
- <sup>20</sup>S. R. Granter, A. H. Beck, and D. J. Papke, "Alphago, deep learning, and the future of the human microscopist," *Arch Pathol Lab Med* **141**, 619–621 (2017).
- <sup>21</sup>A. E. Sallab, M. Abdou, E. Perot, and S. Yogamani, "Deep reinforcement learning framework for autonomous driving," *Electronic Imaging* **29**, 70–76 (2017).
- <sup>22</sup>W. Zhao, J. P. Queralta, and T. Westerlund, "Sim-to-real transfer in deep reinforcement learning for robotics: a survey," in *2020 IEEE Symposium Series on Computational Intelligence (SSCI)* (2020) pp. 737–744.
- <sup>23</sup>P. Garnier, J. Viquerat, J. Rabault, A. Larcher, A. Kuhnle, and E. Hachem, "A review on deep reinforcement learning for fluid mechanics," *Computers & Fluids* **225**, 104973 (2021).
- <sup>24</sup>S. Razdan and S. Shah, "Optimization of fluid modeling and flow control processes using machine learning: A brief review," in *Advances in Mechanical Engineering and Material Science*, edited by K. C. Popat, S. Kanagaraj, P. S. R. Sreekanth, and V. M. R. Kumar (Springer Nature Singapore, Singapore, 2022) pp. 63–85.
- <sup>25</sup>F. Xie, C. Zheng, T. Ji, X. Zhang, R. Bi, H. Zhou, and Y. Zheng, "Deep reinforcement learning: A new beacon for intelligent active flow control," *Aerospace Research Communications* **1** (2023), 10.3389/arc.2023.11130.
- <sup>26</sup>J. Zhao, W. Zhao, B. Deng, Z. Wang, F. Zhang, W. Zheng, W. Cao, J. Nan, Y. Lian, and A. F. Burke, "Autonomous driving system: A comprehensive survey," *Expert Systems with Applications* **242**, 122836 (2024).
- <sup>27</sup>A. Husen, M. H. Chaudary, and F. Ahmad, "A survey on requirements of future intelligent networks: Solutions and future research directions," *ACM Comput. Surv.* **55** (2022), 10.1145/3524106.
- <sup>28</sup>S. Bholra, S. Pawar, P. Balaprakash, and R. Maulik, "Multi-fidelity reinforcement learning framework for shape optimization," *Journal of Computational Physics* **482**, 112018 (2023).
- <sup>29</sup>R. Vinuesa, O. Lehmkuhl, A. Lozano-Durán, and J. Rabault, "Flow control in wings and discovery of novel approaches via deep reinforcement learning," *Fluids* **7**, 62 (2022).
- <sup>30</sup>C. Vignon, J. Rabault, and R. Vinuesa, "Recent advances in applying deep reinforcement learning for flow control: Perspectives and future directions," *Physics of Fluids* **35**, 031301 (2023).
- <sup>31</sup>J. Viquerat, P. Meliga, A. Larcher, and E. Hachem, "A review on deep reinforcement learning for fluid mechanics: An update," *Physics of Fluids* **34** (2022), 10.1063/5.0128446.
- <sup>32</sup>R. Vinuesa, "Perspectives on predicting and controlling turbulent flows through deep learning," *Physics of Fluids* **36**, 031401 (2024).
- <sup>33</sup>J. Rabault, M. Kuchta, A. Jensen, U. Réglade, and N. Cerardi, "Artificial neural networks trained through deep reinforcement learning discover control strategies for active flow control," *Journal of fluid mechanics* **865**, 281–302 (2019).
- <sup>34</sup>H. Tang, J. Rabault, A. Kuhnle, Y. Wang, and T. Wang, "Robust active flow control over a range of Reynolds numbers using an artificial neural network trained through deep reinforcement learning," *Physics of Fluids* **32**, 053605 (2020).
- <sup>35</sup>N. Heess, D. TB, S. Sriram, J. Lemmon, J. Merel, G. Wayne, Y. Tassa, T. Erez, Z. Wang, S. M. A. Eslami, M. Riedmiller, and D. Silver, "Emergence of locomotion behaviours in rich environments," arXiv preprint arXiv:1707.02286 (2017), arXiv:1707.02286 [cs.AI].
- <sup>36</sup>F. Ren, J. Rabault, and H. Tang, "Applying deep reinforcement learning to active flow control in turbulent conditions," *Physics of Fluids* **33**, 037121 (2021), 2006.10683 [physics].
- <sup>37</sup>J. Wang and H. Xu, "Optimal parallelization strategies for active flow control in deep reinforcement learning-based computational fluid dynamics," *Physics of Fluids* **36**, 043623 (2024).

- <sup>38</sup>J. Li and M. Zhang, “Reinforcement-learning-based control of confined cylinder wakes with stability analyses,” *Journal of Fluid Mechanics* **932**, A44 (2022), 2111.07498 [physics].
- <sup>39</sup>Q. Wang, L. Yan, G. Hu, C. Li, Y. Xiao, H. Xiong, J. Rabault, and B. R. Noack, “DRLinFluids: An open-source Python platform of coupling deep reinforcement learning and OpenFOAM,” *Physics of Fluids* **34**, 081801 (2022).
- <sup>40</sup>W. Jia and H. Xu, “Robust and adaptive deep reinforcement learning for enhancing flow control around a square cylinder with varying reynolds numbers,” (2024), arXiv:2404.12123 [physics.flu-dyn].
- <sup>41</sup>B. Wang, Q. Wang, Q. Zhou, and Y. Liu, “Active control of flow past an elliptic cylinder using an artificial neural network trained by deep reinforcement learning,” *Applied Mathematics and Mechanics-English Edition* **43**, 1921–1934 (2022).
- <sup>42</sup>D. Fan, L. Yang, Z. Wang, M. S. Triantafyllou, and G. E. Karniadakis, “Reinforcement learning for bluff body active flow control in experiments and simulations,” *Proceedings of the National Academy of Sciences* **117**, 26091–26098 (2020).
- <sup>43</sup>F. Ren, C. Wang, and H. Tang, “Bluff body uses deep-reinforcement-learning trained active flow control to achieve hydrodynamic stealth,” *Physics of Fluids* **33**, 093602 (2021).
- <sup>44</sup>J. Rabault, F. Ren, W. Zhang, H. Tang, and H. Xu, “Deep reinforcement learning in fluid mechanics: A promising method for both active flow control and shape optimization,” *Journal of Hydrodynamics* **32**, 234–246 (2020).
- <sup>45</sup>H. Jasak, “OpenFOAM: Open source CFD in research and industry,” *International Journal of Naval Architecture and Ocean Engineering* **1**, 89–94 (2009).
- <sup>46</sup>H. Jasak, A. Jemcov, Z. Tukovic, *et al.*, “Openfoam: A c++ library for complex physics simulations,” in *International Workshop on Coupled Methods in Numerical Dynamics*, Vol. 1000 (2007) pp. 1–20.
- <sup>47</sup>M. Schäfer, S. Turek, F. Durst, E. Krause, and R. Rannacher, “Benchmark computations of laminar flow around a cylinder,” in *Flow Simulation with High-Performance Computers II*, Notes on Numerical Fluid Mechanics (NNFM), Vol. 48, edited by E. H. Hirschel (Vieweg+Teubner Verlag, 1996) pp. 547–566.
- <sup>48</sup>M. Schaarschmidt, A. Kuhnle, B. Ellis, K. Fricke, F. Gessert, and E. Yoneki, “LIFT: Reinforcement learning in computer systems by learning from demonstrations,” (2018), arXiv:1808.07903.
- <sup>49</sup>M. Abadi, P. Barham, J. Chen, Z. Chen, A. Davis, J. Dean, M. Devin, S. Ghemawat, G. Irving, M. Isard, M. Kudlur, J. Levenberg, R. Monga, S. Moore, D. G. Murray, B. Steiner, P. Tucker, V. Vasudevan, P. Warden, M. Wicke, Y. Yu, and X. Zheng, “TensorFlow: A system for Large-Scale machine learning,” in *12th USENIX Symposium on Operating Systems Design and Implementation (OSDI 16)* (USENIX Association, Savannah, GA, 2016) pp. 265–283.
- <sup>50</sup>G. Brockman, V. Cheung, L. Pettersson, J. Schneider, J. Schulman, J. Tang, and W. Zaremba, “Openai gym,” (2016), arXiv:1606.01540 [cs.LG].
- <sup>51</sup>J. Rabault and A. Kuhnle, “Accelerating deep reinforcement learning strategies of flow control through a multi-environment approach,” *Physics of Fluids* **31**, 094105 (2019).
- <sup>52</sup>S. A. Johnson, M. C. Thompson, and K. Hourigan, “Predicted low frequency structures in the wake of elliptical cylinders,” *European Journal of Mechanics - B/Fluids* **23**, 229–239 (2004), bluff Body Wakes and Vortex-Induced Vibrations.
- <sup>53</sup>M. Sahin and R. G. Owens, “A numerical investigation of wall effects up to high blockage ratios on two-dimensional flow past a confined circular cylinder,” *Physics of Fluids* **16**, 1305–1320 (2004).
- <sup>54</sup>M. Pastoor, L. Henning, B. R. Noack, R. King, and G. Tadmor, “Feedback shear layer control for bluff body drag reduction,” *Journal of Fluid Mechanics* **608**, 161–196 (2008).
- <sup>55</sup>B. Protas and J. E. Wesfreid, “Drag force in the open-loop control of the cylinder wake in the laminar regime,” *Physics of Fluids* **14**, 810–826 (2002).
- <sup>56</sup>M. Bergmann, L. Cordier, and J.-P. Brancher, “Optimal rotary control of the cylinder wake using proper orthogonal decomposition reduced-order model,” *Physics of Fluids* **17**, 097101 (2005).
- <sup>57</sup>J. Rabault and A. Kuhnle, “Cylinder2dflowcontroldrparallel,” GitHub. <https://github.com/jerabaul29/Cylinder2DFlowControlDRLParallel> (2019).
- <sup>58</sup>J. Li, “RLcontrolnek5000,” GitHub. [https://github.com/npuljc/RL\\_control\\_Nek5000](https://github.com/npuljc/RL_control_Nek5000) (2021).
- <sup>59</sup>W. C. Qiulei Wang, Lei Yan, “Drlinfluids,” GitHub. <https://github.com/venturi123/DRLinFluids> (2022).